Acta Pharmaceutica Sinica B 2026;16(6):3963−3984

Chinese Pharmaceutical Association
Institute of Materia Medica, Chinese Academy of Medical Sciences

Acta Pharmaceutica Sinica B

www.elsevier.com/locate/apsb
www.sciencedirect.com

ORIGINAL ARTICLE

Discovery and mutasynthetic optimization of ansatrienin B: A new broad-spectrum inhibitor against RNA viruses

Xu Zheng[a,†], Hongji Li[a,†], Mengxue Zhang[a,†], Zhiyue Qiu[b,c,d], Xingchi Yang[a], Ziwei Zhou[b], Wei Wu[a], Dunning Yu[a], Xiaofan Zhu[a], Zhiyong Chu[a], Haoran Peng[a], Cuiling Ding[a], Ping Zhao[a], Wen Liu[e], Wanchao Yin[b,c,d], Yangang Liu[a,*], Peng Sun[a,*]

[a]*School of Pharmacy, Department of Microbiology, Faculty of Naval Medicine, Naval Medical University, Shanghai 200433, China*
[b]*Zhongshan Institute for Drug Discovery, Shanghai Institute of Materia Medica, Chinese Academy of Sciences, Zhongshan 528449, China*
[c]*Center for Structure and Function of Drug Targets, Shanghai Institute of Materia Medica, Chinese Academy of Sciences, Shanghai 201203, China*
[d]*University of Chinese Academy of Sciences, Beijing 100049, China*
[e]*State Key Laboratory of Bioorganic and Natural Products Chemistry, Center for Excellence in Molecular Synthesis, Shanghai Institute of Organic Chemistry, University of Chinese Academy of Sciences, Shanghai 200032, China*

Received 21 July 2025; received in revised form 31 December 2025; accepted 14 February 2026

KEY WORDS

Ansatrienin;
Natural product;
RNA virus;
Broad-spectrum antiviral;
SARS-CoV-2;
West Nile virus;
RdRp;
Mutasynthesis

Abstract RNA viruses, such as severe acute respiratory syndrome coronavirus 2 (SARS-CoV-2), flaviviruses, and alphaviruses, represent a major source of emerging human infectious diseases. They pose a persistent threat to public health; however, few therapeutic options are available for severe infections. Through a natural product screening campaign, we identified ansatrienin B as a broad-spectrum inhibitor of multiple RNA viruses, including SARS-CoV-2, flaviviruses (*e.g.*, YFV, WNV, DENV), and alphaviruses (*e.g.*, CHIKV). Time-of-drug-addition assays indicated that ansatrienin B acts at both the early (entry) and intermediate (replication) stages of the viral life cycle. Surface plasmon resonance (SPR) and molecular docking studies validated a direct interaction between ansatrienin B and the

*Corresponding authors.
E-mail addresses: lyg@smmu.edu.cn (Yangang Liu), sunpeng78@126.com (Peng Sun).
[†]These authors made equal contributions to this work.
Peer review under the responsibility of Chinese Pharmaceutical Association and Institute of Materia Medica, Chinese Academy of Medical Sciences.

https://doi.org/10.1016/j.apsb.2026.02.021

RNA-dependent RNA polymerase (RdRp) of SARS-CoV-2 and WNV. Combined RNA pull-down and RdRp enzymatic activity assays (in gel, solution, and cellular forms) further demonstrated that ansatrienin B disrupts both the binding of RdRp to viral RNA and its enzymatic activity. *In vivo*, ansatrienin B showed significant efficacy in mouse models infected with SARS-CoV-2 or WNV infection. To facilitate screening and elucidate the structure−activity relationship (SAR), we generated a focused ansatrienin library *via* a mutasynthetic approach. Supplementation of four 3,5-AHBA analogs into a *ΔmycB1-B4* mutant strain of *Streptomyces flaveolus* yielded 30 novel ansatrienin derivatives. Evaluation of anti-SARS-CoV-2 activity identified four analogs with enhanced potency, enabling the establishment of a preliminary SAR. Collectively, these findings establish ansatrienin B as a novel inhibitor targeting RdRp and provide a foundation for the development alternative broad-spectrum antiviral agents.

1. Introduction

RNA viruses are the most common cause of emerging human infectious diseases, with several well-known vector-borne or zoonotic viral diseases including Zika virus, coronaviruses virus (CoV), Ebola virus (EBOV), West Nile virus (WNV), dengue virus (DENV), and chikungunya virus (CHIKV)[1]. The threat to global public health posed by RNA virus infection persists. The recent coronavirus disease 2019 (COVID-19) pandemic caused by SARS-CoV-2 has resulted in a significant public health crisis and lasting global impacts[2]. Likewise, many new and re-emerging viruses, such as flaviviruses and alphaviruses, continue to have a serious impact on human health. For instance, WNV in the United States and Europe causes periodic outbreaks associated with severe cases of neuroinvasive disease[3]. DENV causes major epidemics in Asia, with an estimated 390 million cases per year[4]. CHIKV causes at least 3 million infections annually in the equatorial regions[5]. So far, however, few effective antiviral therapies are available.

Extensive efforts have been made to address the urgent need for prevention and treatment of COVID-19. Three classes of antiviral drugs have been identified: small-molecule inhibitors, mAbs targeting the spike protein, and several therapies targeting host proteins. The small-molecule antiviral agents include RNA-dependent RNA polymerase (RdRp) inhibitors (VV116, remdesivir, JT001, and molnupiravir) and 3CL protease inhibitors (nirmatrelvir, ensitrelvir, leritrelvir, and simnotrelvir)[6-8]. Notwithstanding the availability of efficacious vaccines and antivirals, the emergence of SARS-CoV-2 variants heightens the need for the development of novel antiviral drugs[6,7]. Flaviviruses and alphaviruses are positive single-stranded RNA viruses transmitted primarily through the bite of infected mosquitoes. The absence of efficacious vaccines or therapeutic agents has raised a considerable public concern[4,5]. Therefore, the development of broad-spectrum antiviral agents against emerging RNA viruses, particularly those with high mutation rates, is vital.

Natural products (NPs) have contributed substantially to the development of new drugs in recent decades. NPs offer several unique advantages including unique structures, diverse bioactivities, and multiple targets, making them worthy of further study for antiviral development. NPs have demonstrated considerable potential for the treatment of RNA virus pathogens and warrant thorough investigation[1,9]. Efforts have been made to identify and assess potential anti-SARS-CoV-2 agents derived from NPs through *in silico* screening and *in vitro* cell-based experiments. Various NPs, including flavonoids, polyphenols, terpenes, and sterols have been confirmed to exert anti-SARS-CoV-2 activity[10,11]. Natural extracts such as polyphenolic compounds delphinidin and epigallocatechin gallate effectively reduce DENV, WNV, and Zika virus infectivity[12].

Ansatrienins belong to a subgroup of the ansamycin family and are characterized by a 21-membered macrolactam skeleton, three conjugated double bonds, and a cyclohexanecarboxylic (CHC) side chain[13,14]. They demonstrate significant biological activities, including anticancer, antimicrobial, and anti-inflammatory effects. In our previous study, we identified ansatrienin B as the major metabolite produced by *Streptomyces flaveolus* and elucidated its biosynthetic gene cluster (BGC)[15,16]. Biosynthetically, the ansatrienin scaffold is assembled by type I polyketide synthase (PKS), with 3-amino-5-hydroxy benzoic acid (3,5-AHBA) serving as the starter unit[17].

In this study, we demonstrated that ansatrienin B has broad-spectrum antiviral efficacy against a range of RNA viruses including SARS-CoV-2, variants of concern, flaviviruses, and alphaviruses. Subsequently, antiviral efficacy was confirmed in animal models of SARS-CoV-2 and WNV infections. Furthermore, the antiviral mechanism of ansatrienin B was investigated using time-of-drug-addition assay, SPR, RNA pull-down assay, and *in vitro* RdRp activity assays. By supplementing 3,5-AHBA analogs into the *ΔmycB1-B4* mutant strain of *S. flaveolus*, we constructed a specific ansatrienin library, and accordingly investigated the structure−activity relationship. Taken together, our results position ansatrienin B as a promising broad-spectrum antiviral candidate, particularly against emerging RNA viruses that utilize a conserved RdRp mechanism.

2. Materials and methods

2.1. Chemical reagents

Biochemicals, restriction enzymes, and media were purchased from Sinopharm Chemical Reagent, Titan, Oxoid, or Thermo Fisher Scientific. PCR amplifications were carried out on a T100 thermal cycler (Bio-Rad) using T5 DNA polymerase or I-5 High-Fidelity Master Mix. Primer synthesis and general DNA sequencing were carried out by Shanghai Sangon Biotech. SARS-CoV-2 RdRp protein was obtained from MedChemExpress (China), which is expressed by Sf9 insect cells with a C-His labeled tag. Materials and reagents used for SPR assays included

Series S NTA sensor chips, 1-(3-dimethylaminopropyl)-3-ethylcarbodiimide hydrochloride (EDC), *N*-hydroxysuccinimide (NHS), and ethanolamine, all of which were purchased from Cytiva (USA).

2.2. Cells and viruses

The African green monkey kidney cell line Vero E6 (Cell Bank of the Chinese Academy of Sciences, Shanghai, China), human epithelial colorectal adenocarcinoma cell line Caco-2, and human cervical cancer cell lines overexpressing human ACE2 (Hela-ACE2) were maintained in Gibco Dulbecco's Modified Eagle Medium (DMEM) supplemented with 10% fetal bovine serum (FBS), 1% non-essential amino acids, 1% L-glutamine and 1% penicillin/streptomycin at 37 °C in a humidified atmosphere with 5% CO_2. The human lung adenocarcinoma cell line Calu-3 was cultured in Gibco DMEM/F-12 supplemented with 15% FBS and 1% penicillin/streptomycin. Authentic preserved SARS-CoV-2 strains (Wuhan/GenBank accession No. MT622319.1; Omicron BA.2/GenBank accession No. ON965795.1; BA.5/GenBank accession No. PQ213095.1; and BF.7/GenBank accession No. OR793072.1) were isolated from a laboratory-confirmed COVID-19 patient by passaging in Vero E6 cells. The virus working stocks were propagated and titrated in Vero E6 cells in the presence of TPCK-treated trypsin at a concentration of 2 μg/mL, and the virus was stored at −80 °C. WNV infectious clones of the NY2000 strain (AF404756) were synthesized in this laboratory. All experiments involving infectious viruses were performed in the Biosafety Level 3 laboratory of Navy Medical University.

2.3. Dose-response analysis and cytotoxicity assay

Cell lines were plated in a 96-well plate (4×10^4 cells/well). For primary screening of anti-SARS-CoV-2 efficacy, Vero E6 cells were infected with SARS-CoV-2 at a multiplicity of infection (MOI) of 0.1 and simultaneously treated with the indicated compounds at 2.5 μmol/L. After 24 h post infection (hpi), the cells were fixed, and viral protein and cell nuclei were visualized with an immunofluorescence (IF) assay. DMSO was tested as the vehicle control and remdesivir as the positive control. For dose-response analysis, cells were infected with test virus at MOI of 0.1 and then treated with eight 2-fold serial dilutions (20−0.1563 μmol/L) or eleven 2-fold serial dilutions (20−0.0195 μmol/L) of the indicated compounds. The cells were fixed after 24 hpi, then viral proteins and cell nuclei were visualized using an IF assay. For each condition, the percentage of infection was calculated as the ratio of the number of infected cells stained for SARS-CoV-2 N protein to the number of cells stained with DAPI (Sigma−Aldrich). The ratios of SARS-CoV-2-infected cells, cell number, and cellular half-maximal inhibitory concentration (IC_{50}) values are shown as the dose-response analysis. Data are normalized to the average of DMSO-treated wells.

SARS-CoV-2 infection was also detected using quantitative reverse transcription (RT-qPCR) to test viral RNA at 24 hpi. Simultaneously, cells were plated in parallel and continuously exposed to various concentrations of the compounds for 48 h. Cytotoxicity was determined using a Cell Counting Kit-8 (Beyotime). The results were detected using the Synergy H1 microplate reader (BioTek Instruments) with absorbance at 450 nm. The half cytotoxic concentration (CC_{50}) values were calculated using GraphPad Prism 8. All data are presented as mean ± standard deviation (SD) of three independent experiments.

2.4. RNA extraction and RT-qPCR

To evaluate the viral loads (N gene, *RdRp*) and relative expression of inflammatory cytokines/chemokines (*Il-6*, *Il17-a*, *Tnf-α*, *Ifn-g*, *Ifn-b*) and stimulator of interferon genes (*Mx1*, *Isg15*, *Ifi44*), RT-qPCR was performed. Briefly, total RNA was extracted from cell or hamster left lung tissues using TRizol Reagent (Thermo Fisher Scientific). The RNA concentrations and the A260/A280 ratio were then assessed with a multiplate reader (Synergy 2; BioTek). RNA was converted into cDNA using a reverse transcription system (Promega). The cDNA product was used directly for the following RT-qPCR analysis directly, with TB Green Fast RT-qPCR Mix (TaKaRa) and gene specific primers. *β*-Actin expression was used for normalization. Specific primers were designed using Primer 5 software (Premier) and ordered from Shanghai Sangon Biotech. The primers are listed in Supporting Information Table S1.

2.5. IF assay

The infected cells were fixed with methanol. After blocking with 3% bovine serum albumin for 2 h, the cells were incubated with a rabbit anti-SARS-CoV-2 N protein antibody (Sino Biological) for 3−4 h at room temperature. Then, the cells were incubated with an Alexa Fluor 488-conjugated secondary antibody (Thermo Fisher Scientific) for 2 h at room temperature. Finally, PBS supplemented with 0.1 μg/mL DAPI was added to the cells for at least 15 min before imaging. Images were acquired using a Cytation 5 (BioTek) instrument. All the acquired data was analyzed by GraphPad Prism 8.

2.6. Time-of-drug-addition assay

Vero E6 cells were seeded in 96-well plates with a density of 4×10^4 cells/well and incubated with SARS-CoV-2 (MOI = 0.1). After 2 h post-infection, the cell culture medium was removed, and the cells were washed twice with ice-cold PBS. Cells were then treated with the ansatrienin B or remdesivir at a final concentration of 2.5 μmol/L at 2 h before (−2) or 0, 2, 4, 6, 8, 10 h after the supernatants were removed. Then, the infection was qualified 24 h post-inoculation after fixation and staining, with SARS-CoV-2 N protein and cell nuclei were visualized with IF assay. Data were normalized to the average of DMSO-treated wells and presented as mean ± SD of three independent experiments.

2.7. Viral binding and internalization assay

To evaluate virus binding, Vero E6 cells were infected with SARS-CoV-2 at an MOI of 0.1. The cells were then treated with five 2-fold serial dilutions of ansatrienin B (5−0.15625 μmol/L) or vehicle control, and incubated at 4 °C for 2 h. The vehicle control contained the same volume of DMSO as was used to dissolve the corresponding concentrations of ansatrienin B. After discarding the culture medium, cells were washed with cold PBS for three times to remove unbound viruses. The cells were then fixed for IF assay and the total RNA was extracted for RT-qPCR.

To evaluate the effect of ansatrienin B on virions, SARS-CoV-2 was incubated with ansatrienin B (1.25 or 5 μmol/L) for 6 h, followed by 1000-fold dilutions to reduce the effect of high

concentration of the compound. After 24 hpi, the cells were fixed, then SARS-CoV-2 N protein and cell nuclei were visualized by IF assay.

To evaluate virus internalization, Vero E6 cells were incubated with SARS-CoV-2 (MOI = 0.1) at 4 °C for 2 h. The cells were washed 3 times to remove any unbound viruses, followed by incubation with varying concentrations of ansatrienin B at 37 °C for 2 h. The cells were fixed for IF assay and the total RNA was extracted for RT-qPCR.

Fluorescence labelled transferrin (TF) was used to assess internalization under ansatrienin B administration. Labelled TF was incubated with Vero E6 cells in 96-well plates at 37 °C for 6 h in the presence of the indicated concentrations of the compound (1.25 or 5 μmol/L), and solvent was tested as vehicle control. Cells were then fixed for IF assay. Images were acquired using a Cytation 5inst.

2.8. SARS-CoV-2 pseudovirus entry assay

SARS-CoV-2 pseudoparticles (SARS-CoV-2pp) were generated as previously described[18]. Cultured 293T cells were co-transfected with phCMV-SARS-CoV-2 Spike (GenBank accession number QHD43416.1); plenti-EGFP, HIV Gag/Pol, and HIV Rev (pLP2) using Lipofectamine 2000 reagent (Thermo Fisher Scientific). The medium was replaced after 6 h of transfection (6 hpt), and the cell supernatant was collected at 72 hpt. For the analysis of drug treatment, cultured Vero E6 cells were infected with SARS-CoV-2pp (MOI 0.2), either with or without ansatrienin B (2.5 μmol/L). Twelve hours after incubation, the cells were transferred to fresh medium. After 48 h, the cells were fixed and stained with DAPI. The EGFP-positive cells were counted using a Cytation 5.

2.9. Time-of-removal assay

Vero E6 cells were plated in 96-well plates with a density of 4×10^4 cells/well. After 12 h, cells were incubated with ansatrienin B (final concentrations of 1.25 or 5 μmol/L) at 4 °C for 2 h, after which SARS-CoV-2 (MOI = 0.1) was added directly or the cells were washed with DMEM 3 times before addition of SARS-CoV-2. An entry inhibition assay, in which ansatrienin B was co-incubated with SARS-CoV-2 prior to addition to cells, was performed.

2.10. SARS-CoV-2 replication assay

The effect of ansatrienin B on virus replication was examined using a replicon plasmid of the SARS-CoV-2 strain constructed as described previously[19]. 1 μg WT replicon RNA and N protein RNA were co-transfected into Huh-7 cells in 96-well plates using Lipofectamine™ 2000 transfection reagent. Six hours after transfection, the supernatant was replaced with fresh culture medium containing either 2.5 or 0.625 μmol/L of ansatrienin B. The cells were incubated for 24 h, after which they were fixed for IFA, reverse transcription for RT-qPCR, and measured by luciferase assay.

2.11. RNA pull-down based assay

The SARS-CoV-2 genomic RNA was biotin-labelled using EZ-Link Psoralen-PEG3-Biotin (Thermo Fisher Scientific) according to the manufacturer's protocol. Reaction mixtures containing 10 μg of biotin-labeled RNA and 10 μg of SARS-CoV-2 RdRp (with or without 10 μmol/L ansatrienin B) were incubated with 10 μL of streptavidin magnetic beads (HY-K0208, Med ChemExpress) at 4 °C overnight. After six washes with 1 × TBST, RdRp protein in the pulled-down fractions was analyzed by Western blotting.

2.12. Expression and purification of the SARS-CoV-2 RdRp complex

The SARS-CoV-2 RdRp complex was prepared using a method adapted from a previous report[20], as detailed below. In brief, nsp12 was expressed in Sf9 insect cells using a baculovirus system with a C-terminal TEV-His_8 tag. Nsp7 and nsp8 were expressed separately in *E. coli* with His_8 tags. All proteins were purified by Ni-NTA chromatography. The insect-cell expressed nsp12/7/8 complex was purified on Ni-NTA, then supplemented with additional bacterial nsp7/nsp8 to saturate the complex. The final complex was purified by SEC, concentrated to ∼12 mg/mL, and stored at −80 °C.

2.13. Gel-based enzymatic activity assay for SARS-CoV-2 RdRp

To conduct the SARS-CoV-2 RdRp enzymatic activity assay, the RNA duplex (primer-template) was prepared as described previously[21]. In brief, a short 5′-FAM-labeled RNA oligonucleotide (5′-FAM-GCUAUGUGAGAUUAAGUUAU-3′) served as the primer, and a longer, unlabeled RNA oligonucleotide (5′-AAAAAAAAAAAUAACUUAAUCUCACAUAGC-3′) served as the template. To form the RNA duplex, equimolar amounts of the primer and template oligonucleotides were combined in annealing buffer (10 mmol/L Tris−HCl, pH 8.0, 25 mmol/L NaCl, 2.5 mmol/L EDTA). The mixture was denatured at 94 °C for 5 min and then gradually cooled to room temperature to facilitate annealing. The purified SARS-CoV-2 RdRp complex (final concentration: 1 μmol/L) was incubated with 3.0 μmol/L dsRNA substrate and 10 mmol/L ATP in a reaction mixture containing 1.14 U/μL RNase inhibitor and reaction buffer (20 mmol/L Tris−HCl, pH 8.0, 10 mmol/L KCl, 6 mmol/L $MgCl_2$, 0.01% Triton X-100, 1 mmol/L DTT). All solutions were prepared using DEPC-treated water. The total reaction volume was 20 μL. After a 60-min incubation in a 37 °C water bath, reactions were terminated by adding 40 μL of quench buffer (94% formamide, 30 mmol/L EDTA in DEPC-treated water). An 18 μL aliquot of the reaction mixture was combined with 2 μL of 10 × DNA loading buffer. Half of this mixture (10 μL) was resolved on a 10% denaturing urea-PAGE gel at 120 V for 1.5 h and visualized using a Tanon-5200 Multi Fluorescence Imager. The protocol for the RdRp inhibition assays with ansatrienin B and NF023 was identical to the enzymatic assay described above, with the following modification: inhibitors were added 60 min prior to the initiation of the reaction with 10 mmol/L ATP. Ansatrienin B was tested at final concentrations of 0, 50, 150, and 500 μmol/L, 1.5, 5, and 15 mmol/L. NF023 was tested at final concentrations of 0, 0.1, 3, 10, 30, 100, and 300 μmol/L.

2.14. Solution-based activity assay for SARS-CoV-2 RdRp

A real-time assay to detect SARS-CoV-2 RdRp-mediated RNA synthesis was established using the fluorescent dye SYTO 9 (Promega), which selectively intercalates into double-stranded RNA (dsRNA) but not single-stranded templates. Fluorescence emission was monitored in real time using a Tecan Spark or

equivalent plate reader equipped with 485 nm excitation and 520 nm emission filters. This assay monitors dsRNA synthesis in a reaction utilizing a poly(U) RNA template and ATP as the sole nucleotide substrate. Reactions were conducted in black, low-volume, round-bottom 384-well plates. The standard reaction mixture (20 μL final volume) consisted of: 20 mmol/L Tris−HCl (pH 8.0), 10 mmol/L KCl, 6 mmol/L $MgCl_2$, 180 μmol/L ATP, 0.2 μmol/L poly(U) template−primer RNA, 0.01% Triton X-100, 1 mmol/L DTT, 0.025 U/mL RNase inhibitor (Beyotime), and 0.25 μmol/L SYTO 9 (from a 50 μmol/L stock in TE buffer, pH 7.5). Reactions were initiated by adding SARS-CoV-2 RdRp to a final concentration of 5 μg/mL. Fluorescence was then recorded every minute for 30 min at a constant 37 °C in a thermostatted plate reader. Control reactions included a maximum activity control (DMSO vehicle only) and a minimum background control (no RdRp enzyme). For inhibition assays, reactions containing the standard concentrations of poly(U) template−primer (0.2 μmol/L) and ATP (180 μmol/L) were incubated with serially diluted inhibitors. Fluorescence data are presented as the mean ± SD. Statistical significance was determined by two-way ANOVA using GraphPad Prism software (version 8.0). The Michaelis constant (K_m) was determined by plotting initial reaction velocity against varying concentrations of ATP or single-stranded RNA template, followed by nonlinear regression analysis. The IC_{50} values were derived by fitting the velocity data to a four-parameter logistic (4 PL) model. All kinetic and inhibitory parameters were calculated using SigmaPlot software (version 11.0).

2.15. Cell-based activity assay for WNV RdRp

Cell-based assay for evaluating the activity on WNV RdRp was conducted using a method described by Cen et al[22]. Briefly, the *in vitro*-transcribed WNV replicon RNA (structure: 5′-UTR-NanoLuc-NS1/2A/2B/3/4A/4B/5-3′-UTR) was transfected into Huh7 cells stably expressing WNV NS5 ($Huh7^{WNV-NS5}$) or control vector ($Huh7^{Vector}$). Six hours post-transfection, the cells were treated with either ansatrienin B (20 μmol/L) or an equivalent volume of DMSO (vehicle control). At 24 h post-transfection, luciferase activity was measured using a luciferase substrate (the relative gray values were scanned with ImageJ), and the levels of WNV replicon RNA were quantified by RT-PCR.

2.16. SPR binding assay

A SPR assay was performed in a BIAcore T200 or 8K biosensors (GE Healthcare) as described previously[23]. Compounds were diluted in PBS with 5% DMSO at the indicated concentrations. The viral proteins were immobilized on a Series S sensor chip NTA (Cytiba). The carboxylic groups of the chip were activated by EDC 0.2 mol/L and NHS 0.05 mol/L. The exceeding active groups were inactivated with 1 mol/L ethanolamine. Analytes were prepared as 2-fold dilutions of indicated concentrations after the pilot experiments, and injected at a flow rate of 30 μL/min at 25 °C. The concentrations for SARS-CoV-2 RdRp ranged from 0.1 to 50 μg/mL in dilution of PBS containing 5% DMSO. The binding time and the association time was 60 s, respectively. The signal responses of the compound solutions were recorded, and the signal of the solution without compounds was utilized as a blank control. SPR assay of ansatrienin B with WNV NS5 was performed on a BIAcore 8K system, with the binding time and the dissociation time of 120 s, respectively. The binding kinetics were analyzed with BIAcore Insight Evaluation software 3.0.12.15655 to obtain the affinity constant (K_D), using at least five-point serial concentrations[23].

2.17. Molecular docking study

Molecular docking studies were carried out using AutoDock Vina 1.1.2 software[24]. The crystal structures of SARS-CoV-2 RdRp and WNV RdRp (NS5) were obtained from the Protein Data Bank with the IDs of 7BV2 and 2HCN, respectively. The structures of ansatrienin B and its analogs were subjected to energy minimization employing the MMFF94 force field. The protein was prepared by using PyMol 2.5.4 software[25], including the removal of water molecules, salts, and non-liganded small molecules, and adding missing hydrogen atoms. The docking box was defined to envelop the active pocket of the protein. ADFRsuite 1.0 was utilized to convert the PDB format of receptor protein into PDBQT format[26]. The docking was conducted with a conformational search exhaustiveness set to 32, while the remaining parameters at default settings. The conformation with the highest affinity score was selected and then visualized using PyMol 2.5.4[25].

2.18. In vivo evaluation of ansatrienin B

All procedures involving animals were reviewed and approved by the Institutional Committee for Animal Care and Biosafety of Naval Medical University. All experiments complied with the relevant ethical regulations. For assess to anti-SARS-CoV-2 activity, the six weeks-old Syrian golden hamsters were purchased from Beijing Vital River Laboratory Animal Technology Co., Ltd. (Beijing, China). For the animal experiments, the hamsters (6 hamster per group) were challenged *via* intranasal (i.n.) injection with inoculation of 10^5 TCID50 SARS-CoV-2 in 80 μL DMEM or PBS followed by daily intraperitoneal (i.p.) administration of solvent buffer (vehicle control), or ansatrienin B (6 mg/kg/day), or remdesivir (6 mg/kg/day), respectively for 5 days (Days −1 to 3). Solvent buffer included 10% DMSO, 40% PEG300, 5% Tween-80, and 45% saline. Test compounds were dissolved by solvent buffer and administrated in specified amounts. Three hamsters were monitored daily for body weights for 14 days. The other three hamsters per group were sacrificed at 4 days post infection, and their lungs were collected for virus loads evaluation, cytokine detection, and pathological examinations.

To detect anti-WNV activity, six-week-old C57BL/6 mice were divided randomly into three groups (13 mice per group) and inoculated *via* i.p. injection with 10^4 plaque-forming units (PFUs) of WNV NY2000 or PBS followed by i.p. administration of solvent buffer (vehicle control) or ansatrienin B (10 mg/kg/day) in solvent, respectively. The drugs (including DMSO) were continued daily for 5 days (Days −1 to 3). The survival and body weight of the mice were monitored daily for 16 days post-WNV inoculation. On the 4th day post infection (4 dpi), brains were obtained from 3 sacrificed mice per group, lysed with TRIzol for virus load *via* RT-qPCR, or ground in cold PBS for assessment of viral titer *via* plaque assay. The vehicle control and the treatment group were designated as same as those in anti-SARS-CoV-2 activity assay.

2.19. Histopathological examination

For histopathology, the right lung was removed, immersion fixed in 4% paraformaldehyde for 48 h, embedded in paraffin, and cut into 4 μm sections. Hematoxylin and eosin (H&E) staining was

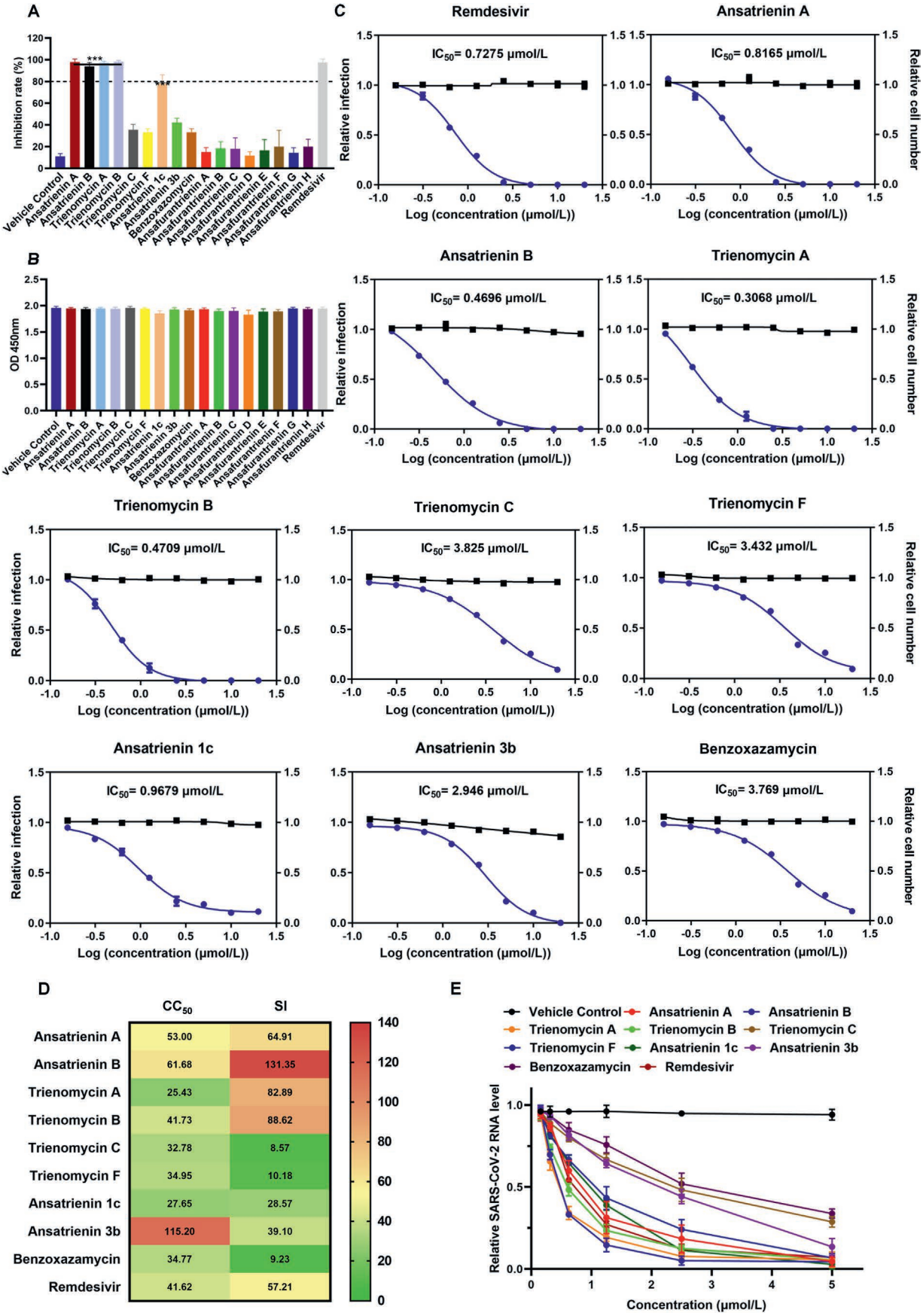
A
Inhibition rate (%)
Vehicle Control
Ansatrienin A
Ansatrienin B
Trienomycin A
Trienomycin B
Trienomycin C
Trienomycin F
Ansatrienin 1c
Ansatrienin 3b
Benzoxazomycin
Ansafurantrienin A
Ansafurantrienin B
Ansafurantrienin C
Ansafurantrienin D
Ansafurantrienin E
Ansafurantrienin F
Ansafurantrienin G
Ansafurantrienin H
Remdesivir
B
OD 450nm
C
Remdesivir
IC50= 0.7275 μmol/L
Ansatrienin A
IC50= 0.8165 μmol/L
Ansatrienin B
IC50= 0.4696 μmol/L
Trienomycin A
IC50= 0.3068 μmol/L
Trienomycin B
IC50= 0.4709 μmol/L
Trienomycin C
IC50= 3.825 μmol/L
Trienomycin F
IC50= 3.432 μmol/L
Ansatrienin 1c
IC50= 0.9679 μmol/L
Ansatrienin 3b
IC50= 2.946 μmol/L
Benzoxazamycin
IC50= 3.769 μmol/L
Relative infection
Relative cell number
Log (concentration (μmol/L))
D
CC50
SI
Ansatrienin A 53.00 64.91
Ansatrienin B 61.68 131.35
Trienomycin A 25.43 82.89
Trienomycin B 41.73 88.62
Trienomycin C 32.78 8.57
Trienomycin F 34.95 10.18
Ansatrienin 1c 27.65 28.57
Ansatrienin 3b 115.20 39.10
Benzoxazamycin 34.77 9.23
Remdesivir 41.62 57.21
E
Vehicle Control
Ansatrienin A
Ansatrienin B
Trienomycin A
Trienomycin B
Trienomycin C
Trienomycin F
Ansatrienin 1c
Ansatrienin 3b
Benzoxazamycin
Remdesivir
Relative SARS-CoV-2 RNA level
Concentration (μmol/L)

performed after dewaxing in xylene and rehydration in decreasing ethanol concentrations. Images were obtained by 200× magnification using a digital microscope system (IX81; Olympus, Japan). The characteristics and severity of the pathologic lesions were scored using lung specific inflammation parameters as previously reported[27]. Three different scores were used that included the following parameters: (i) lung inflammation score including severity of interstitial pneumonia, bronchitis, epithelial necrosis of the bronchi and alveoli, and hyperplasia of type II-alveolar epithelial cells; (ii) immune cell infiltration score taking into account the presence of neutrophils, macrophages, and lymphocytes in the lungs as well as perivascular lymphocytic cuffing; and (iii) edema score, including alveolar edema and perivascular edema.

2.20. Pharmacokinetic (PK) studies

The PK study was performed with adult Sprague−Dawley rats (180−220 g, $n = 3$ per group). Ansatrienin B was administered intravenously (3 mg/kg) or intraperitoneally (6 mg/kg), respectively. Blood samples were collected at 0.083, 0.25, 0.5, 0.75, 1, 2, 4, 8, and 24 h after administration. Plasma was obtained from the blood samples by centrifugation (12,000 rpm for 5 min at 4 °C) and stored at −80 °C before analysis. All samples were quantified by LC−MS/MS.

2.21. Statistical analysis

GraphPad Prism8 was used for statistical tests. Two-tailed Student's *t*-test was used to determine significant *P*-values for comparison of two groups, and one-way ANOVA followed by Tukey or Bonferroni *post-hoc* tests were used for multiple comparisons. Each experiment was repeated at least three times. All data are presented as mean ± SD. *P*-values are indicated by $*P < 0.05$, $**P < 0.01$ and $***P < 0.001$.

2.22. Inactivation of mycB1-B4 in S. flaveolus

The gene inactivation of *mycB1-B4* was carried out using a CRISPR-Cas9 method[28]. The first inserts including specific 20 nt guide sequence were generated by annealing two 34 nt synthesized oligonucleotides, *mycB*-sgRNA-f/*mycB*-sgRNA-r for *mycB1-B4* knock-out in *S. flaveolus*. The annealed fragment was cloned into pMWcas9 at EcoRI/XbaI, generating plasmid pKB001. Two 0.9 kb homologous arm sequences were amplified from genomic DNA using the primer pairs *mycB*-L-f/*mycB*-L-r and *mycB*-R-f/*mycB*-R-r, and then cloned into plasmid pKB001 at HindIII/SpeI by an infusion cloning kit, generating plasmid pKB002 for gene knock-out. The recombination plasmid was confirmed by PCR amplification with primers 2653-f and 2653-r.

The recombinant plasmid was transferred into *E. coli* ET12567 by electroporation. Conjugation between *E. coli* ET12567 and *S. flaveolus* wide type was conducted following the procedure described previously[29]. The plates were incubated for 3−7 days at 30 °C or until conjugates became visible. After conjugation, apramycin resistant exconjugants were subjected to PCR amplification using the primers DB-F/DB-R, which gave a 2.3 kb fragment. Subsequently, 2 μg/mL thiostrepton was used to induce the cleavage of the target DNA in the single crossover recombinants. Next, the induced strains were streaked onto MS agar plate to obtain single colonies, which were further inoculated to a MS agar plate and a MS agar plate containing 50 μg/mL apramycin, respectively. Then, the single colonies that grew only on the plate without antibiotics was inoculated into TSB liquid medium. The genomic DNA was extracted and amplified by PCR using the genotype confirmation primers YB-F/YB-R. Finally, the double crossover recombinants were streaked onto MS agar plates repeatedly to get plasmid free mutant KB002.

DNA isolation and manipulation in *E. coli* or *Streptomyces* strains were carried out according to standard methods. The bacterial strains and plasmids used in gene inactivation are shown in Supporting Information Table S2. Primers used for PCR amplification are shown in Supporting Information Table S3.

2.23. Fermentation, isolation, and structure elucidation of ansatrienin derivatives

The known ansatrienin analogs were obtained from 40 L fermentation of *S. flaveolus* wide type[15]. These analogs include ansatrienin A, B, 1c, 3b, trienomycins A, B, C, F, benzoxazomycin, and ansafurantrienins A−H.

Ansatrienin As−Ds were obtained by feeding experiments. The mutant strain KB002 (*ΔmycB1-B4*) was inoculated in 500 mL Erlenmeyer flask containing 200 mL of seed medium (4.0 g/L glycerol, 1.0 g/L soybean peptone, 2.1 g/L malt extract, pH 7.0) for 2 days and then transferred into 20 L of fermentation medium (4.0 g/L glycerol, 1.9 g/L MES hydrate, 2.0 g/L soybean powder, pH 6.8) at 28 °C and 220 rpm. The feeding precursor (25 mmol/L, DMSO/H_2O 1:1 sterile solution) was added at a volume of 1 mL/flask (200 mL fermentation medium in 1 L flask) at 48 h after inoculation. The fermentation broths were extracted with EtOAc (4 × 20 L) on the fifth day after feeding, and the organic extract was concentrated under reduced pressure to afford a residue. The residue was subjected to MCI column chromatography to obtain different fractions, eluting with a gradient MeOH in H_2O (30%−100%) at 25.0 mL/min. Subsequently, fractions containing the target components were subjected to Sephadex LH-20 column chromatography and RP-HPLC to obtain pure ansatrienin As−Ds.

Structural assignments of new ansatrienin As−Ds were completed by comparison with spectroscopic data of known ansatrienins, and by analyses of multiple spectroscopic experiments including HRMS, 1D and 2D NMR (COSY, HMQC, HMBC, and NOESY). Detailed experiments, procedures and results for isolation and structural elucidation of ansatrienin As−Ds are shown in Supporting Results.

Figure 1 Anti-SARS-CoV-2 efficacy of ansatrienin analogs. (A) Anti-SARS-CoV-2 efficacy of ansatrienin analogs at 2.5 μmol/L in Vero E6 cells. (B) Cytotoxicity of ansatrienin analogs at 10 μmol/L in Vero E6 cells. (C) Dose-response relationship of ansatrienin analogs in Vero E6 cells. Vero E6 cells were treated with eight 2-fold serial dilutions of the indicated compounds and then infected with SARS-CoV-2. (D) Selective index (SI, CC_{50}/IC_{50}) of ansatrienin analogs *in vitro*. (E) Anti-SARS-CoV-2 activity of ansatrienin analogs in Vero E6 cells by RT-qPCR. Data are represented as mean ± SD for three independent experiments. $***P < 0.001$ compared to vehicle control. Vehicle control contained the same volume of DMSO as the corresponding concentrations of labeled compounds.

3. Results

3.1. In vitro antiviral effects of ansatrienin B against SARS-CoV-2

A cell-based screening assay was previously established in Vero E6 cells to identify potential candidates among US Food and Drug Administration-approved drugs for the treatment of COVID-19[30,31]. To identify novel antivirals, this screening assay was employed to assess the inhibitory potential of secondary metabolites from marine invertebrates and microorganisms. Notably, ansatrienin B demonstrated considerable efficacy against SARS-CoV-2 infection (Fig. 1A and C). In addition to ansatrienin B, 16 analogs were co-isolated, including ansatrienins A, 1c, and 3b, trienomycins A-C and F, benzoxazomycin, and ansafurantrienins A-H (Supporting Information Fig. S1). Subsequently, an initial assessment was conducted to evaluate the antiviral effects of ansatrienin analogs on SARS-CoV-2. Specifically, Vero E6 cells were infected with authentic SARS-CoV-2 at an MOI of 0.1 and simultaneously treated with ansatrienin analogs at 2.5 μmol/L. Remdesivir and DMSO were used as the positive and negative controls, respectively. As illustrated in Fig. 1A, ansatrienins A and B and trienomycins A and B showed potent antiviral activity, capable of impeding SARS-CoV-2 infection by more than 80%. Additionally, all ansatrienins had low cytotoxicity at 10 μmol/L (Fig. 1B). The IC_{50} and CC_{50} values of nine ansatrienins against authentic SARS-CoV-2 were subsequently evaluated (Fig. 1C−E and Supporting Information Fig. S2). The working concentration of the test compounds was established at 20 μmol/L, and eight two-fold serial dilutions were performed. All tested ansatrienins exhibited notable inhibitory activities against SARS-CoV-2 infection with IC_{50} values ranging from 0.3068 to 3.8250 μmol/L (Fig. 1C). Five of the compounds, including ansatrienins A, B, and 1c and trienomycins A and B, showed IC_{50} values in the sub-micromolar range, comparable to that of remdesivir. The CC_{50}s of the nine ansatrienins in Vero E6 cells ranged from 25.43 to 115.20 μmol/L (Fig. 1D and Fig. S2). In addition, the selective index (SI) of ansatrienins against SARS-CoV-2 ranged from 8.57 to 131.35, with ansatrienin B exhibiting the highest SI (Fig. 1D). Therefore, the antiviral efficacy of ansatrienin B requires further investigation.

To ascertain the independence of the antiviral activity of ansatrienin B with respect to specific cell lines, the antiviral activity was validated in several other cell lines, including Hela-ACE2 (IC_{50} = 0.5258 μmol/L), Calu-3 (IC_{50} = 0.5792 μmol/L), and Caco-2 (IC_{50} = 0.3982 μmol/L). These results indicated that the compound exerted extensive inhibitory effects on several cell lines derived from different target tissues (Fig. 2A).

3.2. Broad-spectrum antiviral effects of ansatrienin B in vitro

To ascertain whether ansatrienin B could inhibit the replication of various SARS-CoV-2 variants, the efficacy of ansatrienin B against a range of Omicron variants, including BA.2, BA.5, and BF.7, was evaluated. Ansatrienin B exhibited broad inhibitory activity against the SARS-CoV-2 variant of concern, with IC_{50} values ranging from 0.0642 to 0.3050 μmol/L (Fig. 2B). Notably, ansatrienin B demonstrated superior inhibitory activity against Omicron variants compared with the ancestral strains. These results indicate that ansatrienin B exhibits broad-spectrum activity against a range of SARS-CoV-2 variants.

Furthermore, ansatrienin B was also observed to inhibit flaviviruses, including yellow fever virus (YFV), WNV, and DENV, and alphaviruses like CHIKV, in a dose-dependent manner, with IC_{50} values ranging from 0.1450 to 0.5127 μmol/L (Fig. 2C).

3.3. Ansatrienin B inhibits SARS-CoV-2 entry at the viral binding step

To determine the inhibitory effect of ansatrienin B on SARS-CoV-2, a life-cycle analysis was performed using a time-of-addition study. Vero E6 cells were infected with the virus (MOI = 0.1) and treated with ansatrienin B (2.5 μmol/L) for various periods of time. Compared with remdesivir, a known viral replication inhibitor, ansatrienin B exhibited obvious suppressive activity during all periods, with the exception of the pretreatment period, which showed slight inhibition. This indicates that ansatrienin B functions during the early and intermediate stages of SARS-CoV-2 infection, potentially at the entry and replication stages (Fig. 3A).

Viral entry, including the binding and internalization processes, plays a critical role during SARS-CoV-2 infection. Thus, the impact of ansatrienin B on virus entry was examined subsequently. As shown in Fig. 3B and C, ansatrienin B suppressed both viral binding and internalization in a dose dependent manner, especially at the binding stage. Ansatrienin B also showed an inhibitory effect on SARS-CoV-2 pseudoparticle infection, with an approximate inhibition rate of 52.1% (Supporting Information Fig. S3A). A fluorescence-labelled transferrin uptake assay was used to determine whether ansatrienin B influences the classical clathrin-mediated viral internalization. However, no discernible differences were observed in transferrin uptake after ansatrienin B treatment (Fig. S3B), indicating that SARS-CoV-2 internalization may not be the primary mechanism of action of ansatrienin B.

To clarify how ansatrienin B affects viral binding, two distinct binding assays targeting the host or virions were conducted. When SARS-CoV-2 and ansatrienin B were simultaneously added to cells, ansatrienin B blocked SARS-CoV-2 entry (Fig. S3C, blue column). However, when ansatrienin B was added to the cells before infection with SARS-CoV-2, approximately 37.86% and 58.45% of the inhibitory activity was maintained in comparison with the simultaneous operation (Fig. S3D, black column). In contrast, ansatrienin B lost its inhibitory ability when it was first incubated with the target cells and then washed away before the addition of SARS-CoV-2 (Fig. S3C, gray column). These findings indicated that the inhibitory effect of ansatrienin B on viral binding did not rely on the putative effect on host cells. At the same time, no discernible difference in infectivity was observed between the ansatrienin B group and the vehicle group when virions were incubated with ansatrienin B and then subjected to 1000-fold dilutions to reduce the effect of high concentrations of the compound (Fig. S3D). These observations suggest that the inhibitory effect of ansatrienin B may occur during virus-host interactions, specifically at the binding stage, rather than affecting the virion itself or the host cell factors.

3.4. Ansatrienin B suppresses viral replication via potential interaction with RdRp

As shown in Fig. 3A, the inhibition patterns of ansatrienin B and remdesivir were comparable during the post-entry phases, suggesting that ansatrienin B may play a role in the replication stage of viral infection. As a nucleoside analog, remdesivir specifically targets the SARS-CoV-2 RdRp, which is essential for viral replication and represents an attractive antiviral target.

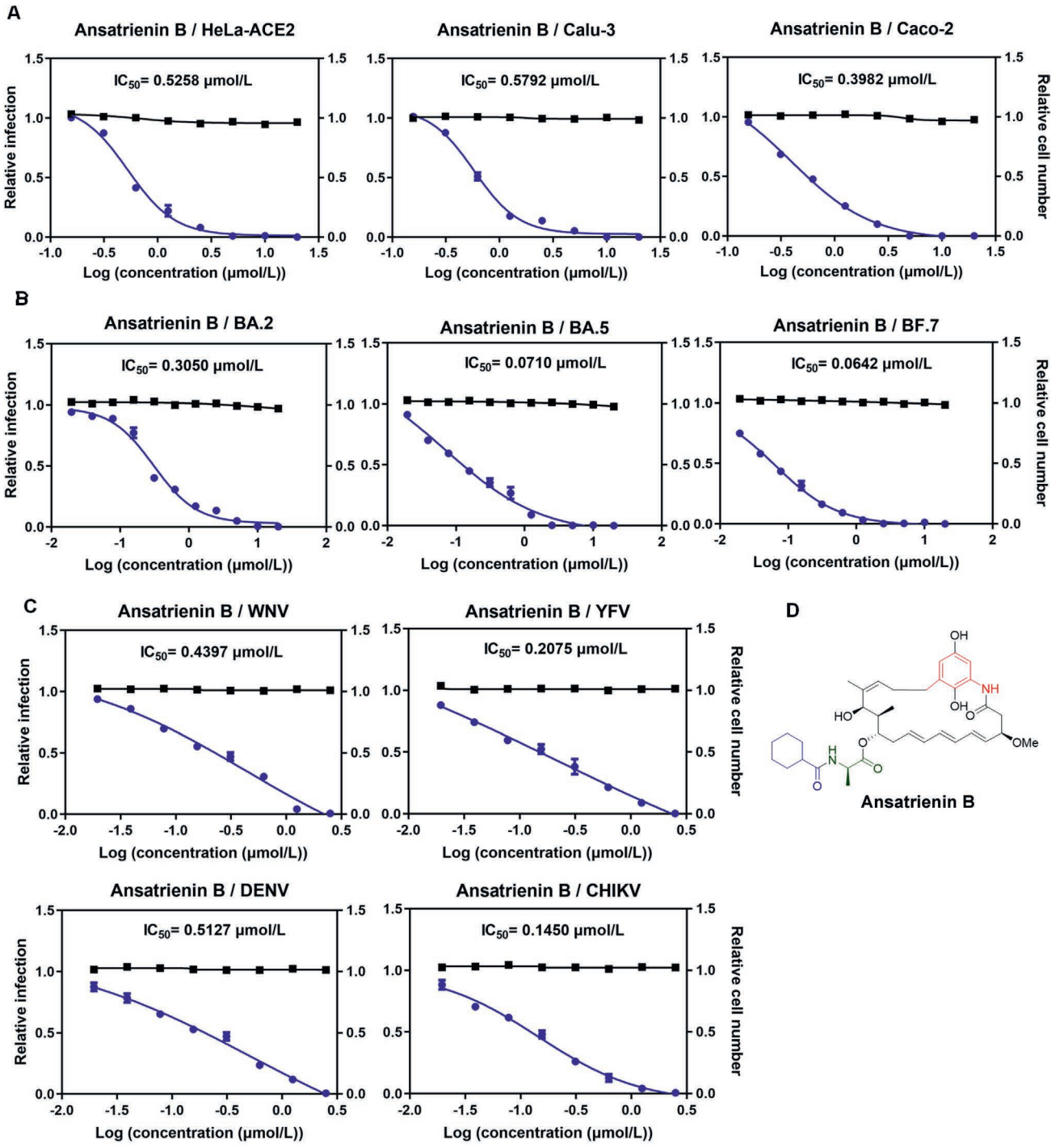

Figure 2 Broad-spectrum antiviral activities of ansatrienin B. (A) Dose-response relationship of ansatrienin B in other cell lines. Hela-ACE2/Calu-3/Caco-2 cells were treated with eight 2-fold serial dilutions of ansatrienin B and then infected with SARS-CoV-2. (B) Dose-response relationship of ansatrienin B against SARS-CoV-2 Omicron variants. Vero-E6 cells were treated with eleven 2-fold serial dilutions of ansatrienin B and then infected with SARS-CoV-2 Omicron variants. (C) Effect of ansatrienin B on flaviviruses (YFV, WNV, DENV) and alphaviruses (CHIKV). Huh7 cells were treated with eight 2-fold serial dilutions (2.5−0.0195 μmol/L) of ansatrienin B and then infected with YFV, WNV, DENV, or CHIKV, respectively. The non-structural (NS) protein and cell nuclei were visualized with an IF assay. (D) Chemical structure of ansatrienin B. Data was represented as mean ± SD for three independent experiments.

Subsequently, the role of ansatrienin B in viral replication and its interaction with RdRp were investigated.

To ascertain the effect of ansatrienin B on the replication of SARS-CoV-2, a SARS-CoV-2 replicon was employed. Notably, ansatrienin B showed superior potency compared with remdesivir in inhibiting SARS-CoV-2 replicon luminescence and viral N-protein expression (Fig. 3D−F). Given the importance of RdRp in RNA virus replication, we examined its role in ansatrienin B

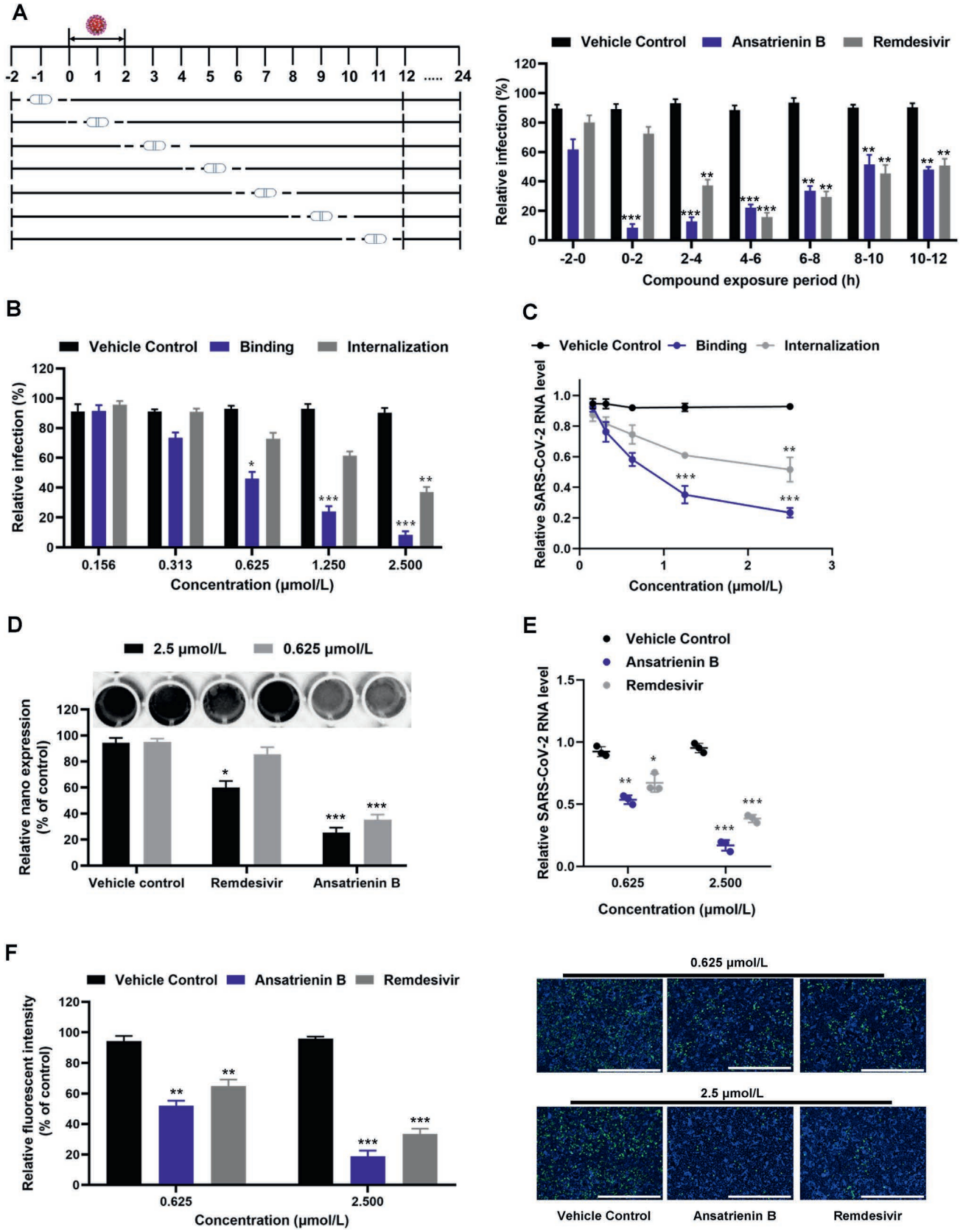

Figure 3 Mechanistic study of ansatrienin B against SARS-CoV-2. (A) Effect of ansatrienin B on SARS-CoV-2 life cycles by a Time-of-addition assay. Vero E6 cells were incubated with SARS-CoV-2 for 2 h to synchronize the assay, then the culture medium was removed. Cells were treated with ansatrienin B or remdesivir at a final concentration of 2.5 μmol/L at 2 h before (−2) or 0, 2, 4, 6, 8, and 10 h after the supernatants were removed. The infection was qualified at 24 h post-inoculation after fixation and staining for SARS-CoV-2 N protein and cell

function. The interaction of the recombinant virus-derived SARS-CoV-2 RdRp protein with ansatrienin B was monitored using an SPR affinity assay. As shown in Fig. 4A, ansatrienin B specifically bound to SARS-CoV-2 RdRp on the sensor surface in a dose-dependent manner with moderate affinity (K_D: 8.8×10^{-5} mol/L). Linoleic acid was used as a positive control (K_D: 5.16×10^{-6} mol/L, Fig. S3E)[32]. Meanwhile, ansatrienin B was able to bind to the WNV RdRp (NS5) protein with a higher affinity (K_D: 5.9×10^{-6} mol/L, Fig. 4B). These findings indicated the existence of a direct binding interaction between ansatrienin B and the RdRp proteins of various RNA viruses.

Molecular docking studies were conducted to predict the interaction patterns between ansatrienin B and RdRp proteins of SARS-CoV-2 (PDB 7BV2) and WNV (2HCN)[20,24]. As illustrated in Fig. 4C, ansatrienin B fitted well into the central pockets of RdRp protein (ΔG: −8.5); the details on the right part of the figure illustrate that the 13-OH, 22-OH, and C-30 carbonyl groups of ansatrienin B form hydrogen bonds with the Ala685, Val560, and Tyr689 residues of the protein, respectively. These residues are involved catalytically active sites or the recognition and binding of the template RNA of SARS-CoV-2 RdRp[20]. This explains how ansatrienin B interferes with the RNA replication of SARS-CoV-2. In addition, ansatrienin B also exhibited a strong interaction with WNV NS5 in molecular docking (ΔG: −8.7). Hydrogen bonds were observed between 13-OH, 22-OH, and 26-OMe functional groups in ansatrienin B and the residues Asp536, Glu738, and Gln710 in WNV NS5 (Fig. 4D). The core structural features of RdRps are highly conserved among various RNA viruses. Direct interaction between ansatrienin B and RdRps may be responsible for their broad-spectrum antiviral activity.

To confirm the impact of ansatrienin B on RdRp function, an RNA pull-down assay was performed to investigate whether ansatrienin B affected the interaction between RdRp and the viral genome. As shown in Fig. 5A and Fig. S3F, the SARS-CoV-2 genome efficiently pulled down the RdRp protein, which was markedly inhibited by ansatrienin B. This confirms that ansatrienin B inhibits the binding of RdRp to SARS-CoV-2 RNA.

The SARS-CoV-2 RdRp comprises the catalytic nonstructural protein nsp12 along with two essential accessory subunits, nsp7 and nsp8. Incubation of the purified nsp12−7−8 complex with a 30-base template and a 20-base primer (poly-U, Fig. S3G) resulted in full-length primer extension to match the template, as visualized by a gel-based assay under saturated ATP conditions (Fig. 5B). The addition of 5 mmol/L ansatrienin B almost completely abolished primer elongation. In contrast, a comparable inhibitory effect required 100 μmol/L NF023. Quantitative analysis using an optimized solution-based inhibition assay determined the IC_{50} value of ansatrienin B to be 0.34 mmol/L (Fig. 5C). Under identical conditions, NF023 exhibited an IC_{50} of 3.42 μmol/L (Fig. S3G and S3H). Notably, the inclusion of excess nsp7 and nsp8 subunits in the assay conditions elevated the observed IC_{50} value for NF023 to 3.42 μmol/L, which is approximately 25-fold higher than the value (0.14 μmol/L) reported in our prior study under different conditions[21]. Therefore, the absolute IC_{50} value for ansatrienin B should be interpreted within this specific assay context and is not a direct reflection of its intrinsic inhibitory potency.

To investigate whether ansatrienin B can inhibit the activity of the WNV RdRp/NS5 in cell culture, we conducted a mini-genome assay based on WNV replicon RNA[22,33]. *In vitro*-transcribed WNV replicon RNA harboring the NanoLuc reporter gene was introduced into the Huh7 cells that stably express WNV NS5 ($Huh7^{WNV-NS5}$) or control vector ($Huh7^{Vector}$), followed by treatment with either ansatrienin B or DMSO (vehicle control). As shown in Fig. 5D and E, NS5 expression robustly enhanced both the replication of WNV replicon RNA and the expression of the NanoLuc reporter gene at 24 h post-transfection, and this promoting effect was reversed by ansatrienin B treatment. Collectively, these results confirmed ansatrienin B as a direct, dose-dependent inhibitor of SARS-CoV-2 and WNV RdRp activity *in vitro*.

3.5. *In vivo anti-SARS-CoV-2 efficacy of ansatrienin B*

The single-dose acute toxicity of ansatrienin B was carried out in healthy mice following previous protocols[34]. The LD_{50} for a single i.p. administration of ansatrienin B in ICR mice was 52.0 mg/kg, with a 95% confidence interval of 46.2−58.6 mg/kg. The prophylactic efficacy (Days 1 to 3; once/daily) of ansatrienin B was determined *in vivo* using Syrian hamsters challenged with authentic SARS-CoV-2[35,36]. The dosage in hamsters was selected based on the safety of LD_{50} and preliminary studies[37]. Each group of Syrian hamsters was administered i.p. ansatrienin B (6 mg/kg/day) or the solvent (vehicle control) one day before each animal was challenged i.n. with 10^5 $TCID_{50}$ of authentic SARS-CoV-2, and then treated daily for 5 consecutive days (Fig. 6A). Compared with the mock group, SARS-CoV-2-infected hamsters exhibited body weight loss from 2 to 8 dpi, whereas the ansatrienin B-treated group showed less weight loss (extreme weight loss 8.25%) and earlier weight recovery (6 dpi) than the vehicle-treated group (16.25% and 8 dpi) (Fig. 6B). Next, the viral load of lung tissue was evaluated to confirm antiviral activity of ansatrienin B. Compared with the vehicle-treated group, the administration of ansatrienin B 1 day before the virus challenge led to robust inhibition of viral replication and viral titers in

nuclei were visualized with IF assay. Remdesivir served as a positive control. (B, C) Effect of ansatrienin B on SARS-CoV-2 entry in Vero E6 cells. Vero E6 cells were treated with vehicle control or ansatrienin B at indicated concentrations, and incubated with SARS-CoV-2 (MOI = 0.1) at 4 °C for 2 h. For binding assay (no incubation) or internalization assay (incubated at 37 °C for another 2 h), cells were washed with cold PBS 3 times to remove unbound viruses. Then, cells were supplemented with growth medium and incubated at 37 °C for 24 h to test the infection by an IF assay. TRIzol reagent was directly added to the 24-well plate to lyse the cells. The total RNA was extracted, and the level of SARS-CoV-2 RNA was detected *via* RT-qPCR. The vehicle control contained the same volume of DMSO as was used to dissolve the corresponding concentrations of ansatrienin B. (D, E) Ansatrienin B suppressed SARS-Cov-2 replication. Vero-E6 cells were transfected with 1 μg of SARS-CoV-2 replicon RNA for 6 h. The culture medium was replaced with fresh medium (vehicle control) or containing ansatrienin B or Remdesivir at indicated concentrations for 24 hpi. Cells were detected *via* luciferase assay, IF and RT-qPCR. (F) A parallel experiment was performed and the expression of replicon was detected using an IF assay. Data are represented as mean ± SD for three independent experiments. $*P < 0.05$, $**P < 0.01$, $***P < 0.001$ compared to vehicle control. Scale bar = 1000 μm.

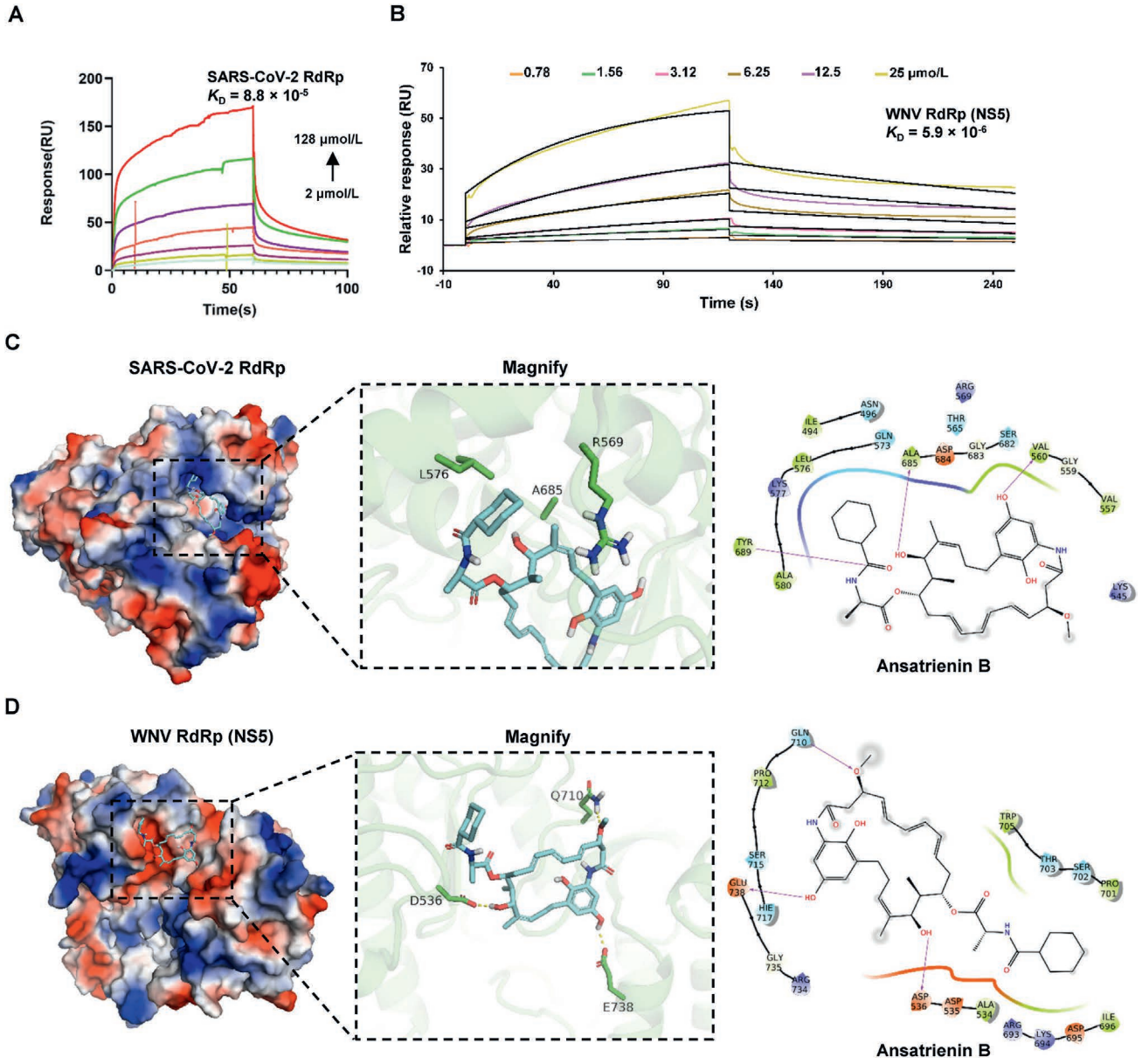

Figure 4 SPR and molecular docking studies of the interaction between ansatrienin B and viral RdRp. (A, B) Evaluation of the binding affinity of ansatrienin B to SARS-CoV-2 RdRp and WNV RdRp by a SPR assay. (C, D) Predicted intermolecular interaction of ansatrienin B and SARS-CoV-2 RdRp (PDB 7BV2) and WNV RdRp (PDB 2HCN). Left are the overall view and binding pocket of RdRp with ansatrienin B; right shows the individual residues lining the pocket. Hydrogen bonds are indicated with pink arrows.

lung tissue (Fig. 6C). SARS-CoV-2 infection of hamsters upregulated the expression of several inflammatory cytokines and stimulated genes in the lungs such as *Tnfa*, *Il-6*, *Ifng*, *Il-17a*, *Ifnb*, *Mx1*, *Isg15*, and *Ifi44*, which were downregulated by the treatment with ansatrienin B at 4 dpi (Fig. 6D). Lung histopathological analysis by H&E staining after SARS-CoV-2 challenge revealed early multifocal damage with accumulation of inflammatory cells, infiltration of macrophages and lymphocytes into the alveolar interstitium and capillaries, and stenosis or even disappearance of alveolar cavities (Fig. 6E, red arrows). Histological scores of the lung tissue indicated that the ansatrienin B group exhibited a more pronounced effect on lung pathological changes than the remdesivir group (Fig. 6F). In conclusion, administration of ansatrienin B prevented inflammation and subsequent damage following viral infection.

3.6. *In vivo anti-flavivirus effect of ansatrienin B*

To assess the *in vivo* anti-flavivirus effect of ansatrienin B, we evaluated its protective effects in mice challenged with WNV. First, to determine whether ansatrienin B could rescue mice from WNV-induced mortality, 6-week-old C57BL/6 mice were inoculated i.p. with a lethal dose of WNV and treated with either vehicle (negative control) or ansatrienin B (10 mg/kg/day) from the day before infection to the third day after infection (−1 to 3 dpi). Body weight and survival of the mice were monitored for 16 days (Fig. 7A). From 6 to 9 dpi, all mice in the vehicle-treated group showed neurological symptoms, including hunched posture, ruffled fur, tremors, and limb paralysis. From 10 to 15 dpi, all mice in the control group succumbed to infection (Fig. 7B, black line). However, in the ansatrienin B group, the symptoms were

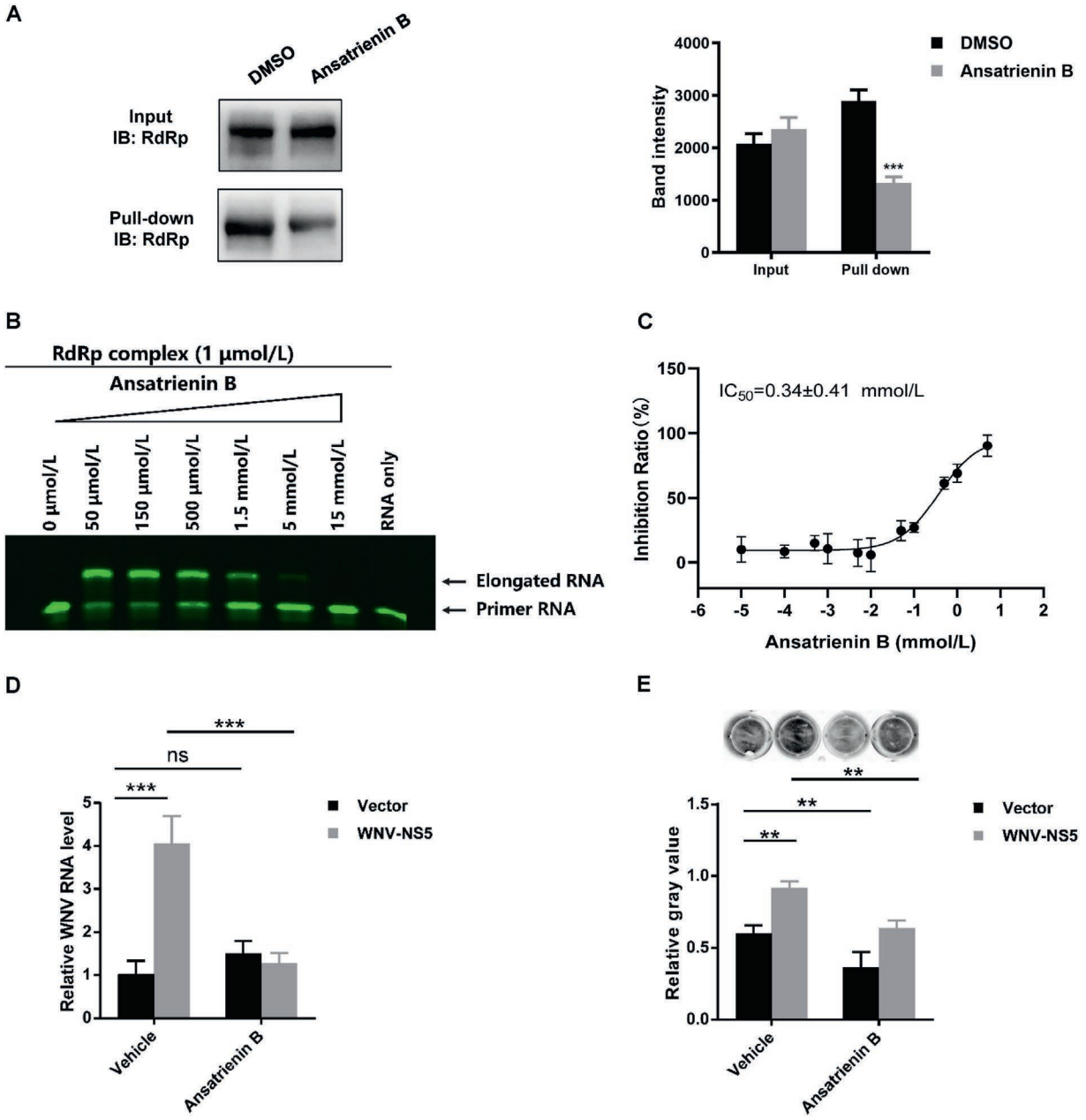

Figure 5 Effect of ansatrienin B with viral RdRp. (A) Ansatrienin B inhibited the interaction between RdRp and SARS-CoV-2 genome. Psoralen-PEG3-Biotin labeled SARS-CoV-2 genomic RNA (10 μg) was mixed with SARS-CoV-2 RdRp (10 μg), ansatrienin B (10 μmol/L), incubated with 10 μL streptavidin magnetic beads at 4 °C overnight and washed, RdRp protein in the pulled-down fractions was analyzed by immuneblotting. The gray intensity of immunoblotting bands was analyzed using ImageJ software. (B) Gel image showed elongation of the RNA duplex by the purified SARS-CoV-2 RdRp complex and its inhibition by ansatrienin B across a concentration range (50 to 15 mmol/L). (C) Quantitative analysis of RdRp inhibition by ansatrienin B. Data are presented as the mean ± SD of four replicates within one experiment. The WNV RdRp inhibition by ansatrienin B was shown as (D) luciferase activity and (E) WNV replicon RNA levels. *In vitro*-transcribed WNV replicon RNA was transfected into Huh7$^{WNV-NS5}$ (WNV-NS5) or Huh7^{Vector} (Vector). Six hours post-transfection, the cells were treated with either ansatrienin B (20 μmol/L) or DMSO (vehicle control). At 24 h post-transfection, luciferase activity was measured using a luciferase substrate (5D), and the levels of WNV replicon RNA were quantified by RT-PCR (5E). ns: no significant; $^{**}P < 0.01$; $^{***}P < 0.001$.

significantly alleviated, and the survival rate improved by 25% (Fig. 7B, blue line). Consistently, ansatrienin B treatment protected mice from WNV infection-induced body weight loss (Fig. 7C). At 4 dpi, the brains of the infected mice were isolated, and the viral load was assessed using plaque assays or RT-qPCR. As expected, repeated administration of ansatrienin B resulted in a marked reduction in the number of live virions (viral titre) and the amount of viral RNA (viral load) in the brain at 4 dpi compared with those in the vehicle group (Fig. 7D). Pathological damage to the tissues of the infected mice was analyzed using H&E staining. As shown in Fig. 7E, obvious pathological alterations were observed in the liver, spleen, kidney, and brain of the vehicle-treated group, including mild granulocyte infiltration (purple arrow), severe hydropic degeneration (blue arrow) in hepatocytes,

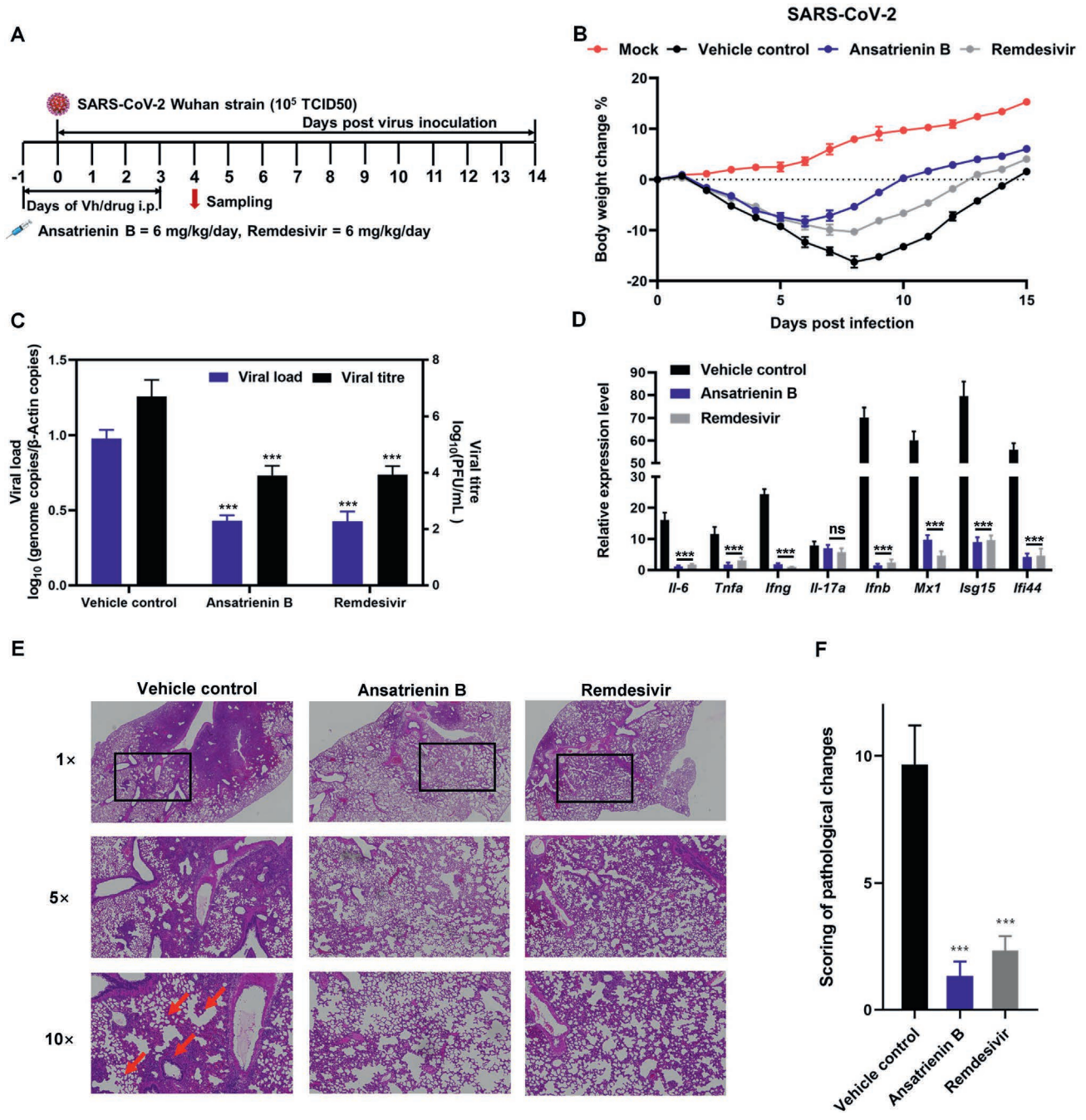

Figure 6 Ansatrienin B protects hamster from SARS-CoV-2 infection-caused injury. (A) Scheme and drug administration of the animal experiment. The hamsters were challenged *via* i.n. injection with inoculation of 10^5 TCID50 SARS-CoV-2 Wuhan strain and followed by daily i.p. administration of solvent buffer or test compounds, respectively, for five days. Three hamsters were monitored daily for body weights. The other three hamsters in each group were sacrificed and sampled four days after infection. (B) Percentage of body weight changes (compared to starting weight) were monitored daily for 15 days. Four groups were included: Mock group (uninfected and i.p. administration of solvent buffer); Vehicle control group (infected with SARS-CoV-2 and i.p. administration of solvent buffer); Ansatrienin B group (infected with SARS-CoV-2 and i.p. administration of ansatrienin B); Remdesivir group (infected with SARS-CoV-2 and i.p. administration of remdesivir). (C, D) Lungs were harvested at 4 dpi and viral load was assessed by plaque assay (viral titre) or RT-qPCR (viral load). The expression of inflammatory cytokines was tested by RT-qPCR. (E) Representative images of H&E-stained lung tissue section from SARS-CoV-2 infected hamsters. Red arrows: sites of inflammatory infiltration and alveolar wall thicken or congestion. (F) Histological analysis of lung pathology. Histology scores were given to each lung tissue to distinguish comprehensive lung pathological changes ($n = 6$). Data are represented as mean ± SD for three independent experiments. ***$P < 0.001$ compared to vehicle control.

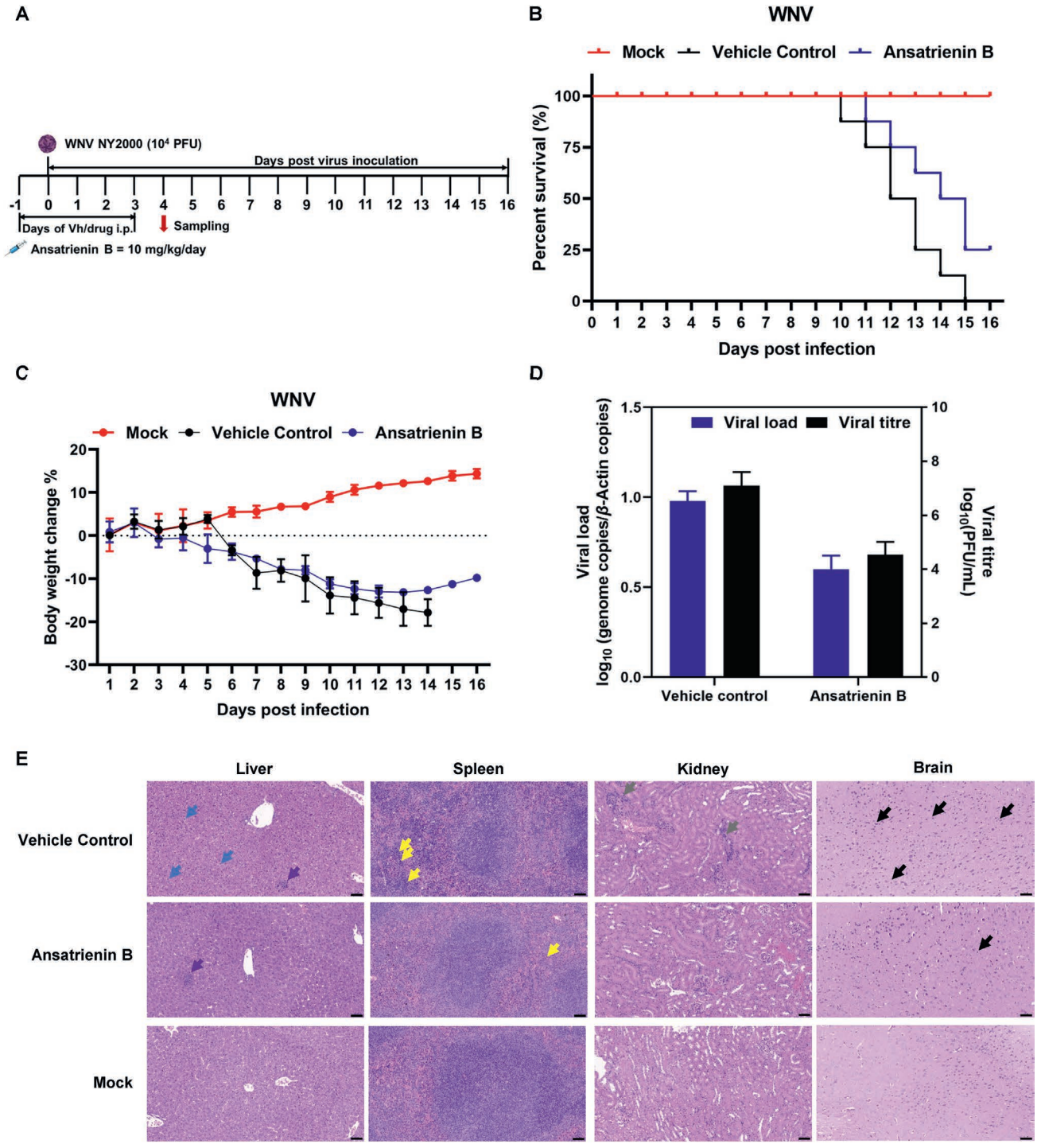

Figure 7 Ansatrienin B reduces WNV infection-caused injury and death in mice. (A) Scheme and drug administration of the animal experiment. Six-week-old C57BL/6 mice were randomly divided into three groups. WNV NY2000 strains (10^4 PFUs) were inoculated, followed by the daily i.p. administration of solvent buffer or ansatrienin B, for five days. The survival and body weight of the mice were monitored daily. On 4 dpi, the livers, spleens, kidneys, and brains of three sacrificed mice per group were obtained for sampling. (B, C) Survival curves and percentage of body weight changes (compared to starting weight) were monitored daily for 16 days. Three groups were included: Mock group (uninfected and i.p. administration of solvent buffer); Vehicle control group (infected with WNV and i.p. administration of solvent buffer); Ansatrienin B group (infected with WNV and i.p. administration of ansatrienin B). (D) Brains were harvested at 4 dpi and viral load was assessed by plaque assay (viral titre) or RT-qPCR (viral load). (E) Representative images of H&E-stained liver, spleen, kidney, and brain tissue section from WNV infected mice. purple arrow: mild granulocyte infiltration; blue arrow: hydropic degeneration; yellow arrows: lymphocytic infiltration in the red pulp of the spleen; gray arrows: lymphocytic infiltration in kidney; black arrow: neurons pyknosis ($n = 13$). Data are represented as mean ± SD for three independent experiments. ***$P < 0.001$ compared to vehicle control. Scale bar = 100 μm.

lymphocytic infiltration in the red pulp of the spleen (yellow arrows) and kidney (gray arrows), and a pyknosis in a large number of neurons in the striatum (black arrow). In comparison, the target organs in the ansatrienin B group exhibited significantly milder pathological changes. These results demonstrate that treatment with ansatrienin B markedly inhibited WNV infection and WNV-induced inflammation *in vivo*.

3.7. PK properties of ansatrienin B in vivo

PK properties of ansatrienin B were investigated in Sprague−Dawley rats. Table 1 summarizes the key PK parameters after a single i.v. and i.p. administration. Following i.v. injection with 3 mg/kg, the half time ($t_{1/2}$), the clearance rate (CL), and apparent distribution volume (V_{ss}) of ansatrienin B were 6.96 h, 147.4 mL/min/kg, and 37.2 mL/kg, respectively. Upon i.p. administration with 6 mg/kg, its $t_{1/2}$, maximum plasma concentration (C_{max}), and area under curve (AUC) were satisfactory as 5.84 h, 178.4 ng/mL, and 777.2 ng h/mL, respectively. The high bioavailability (F, 112.2%) of ansatrienin B in the i.p. group indicated nearly complete absorption, with possible enterohepatic circulation or local retention. The higher AUC_{0-24}/Dose (dose-normalized AUC) in i.p. administration (125.2 ng h/mL) compared with the i.v. group (111.3 ng h/mL) revealed superior overall exposure. However, the lower V_{ss} value indicated that ansatrienin B was primarily distributed in plasma or highly perfused tissues. This may result in limited diffusion from pulmonary capillaries into the lung interstitium and alveoli, leading to insufficient exposure in the lungs.

3.8. Preparation of ansatrienin analogs by mutational synthesis

Given the potential antiviral activity of ansatrienin B, we investigated the possibility of enhancing its antiviral efficacy through structural modification and explored the SAR between ansatrienins and antiviral activity. In the biosynthetic assembly of ansatrienins (Fig. 8A), the PKS proteins (MycD1-D5) together with an amide synthase (MycE) are responsible for the construction of a 21-membered macrolactam[17]. The starter unit 3,5-AHBA is biosynthesized by MycB1-B7 from UDP-glucose. The CHC moiety is synthesized from shikimate using the enzymes MycA1-A4. Post-modifications include O-methylation at C-3 (MycF3), hydroxylation at C-19 (MycF2, an FAD-dependent monooxygenase), D-Ala loading at C-11 (MycC, a standalone NRPS), and *N*-acylation of the CHC moiety (MycF1). Notably, the ansamycin family exhibits remarkable flexibility in starter unit recognition. This has been successfully exploited for generating structural derivatives through mutasynthetic approaches, as demonstrated in the production of geldanamycin and ansamitocin analogs[38-40]. However, despite these advances, mutasynthetic strategies have not yet been applied to ansatrienins. Accordingly, we employed a mutasynthetic approach to prepare new ansatrienin derivatives.

Table 1 PK Property of ansatrienin B after administration in SD rats ($n = 3$).

PK parameters	i.v. (3 mg/kg)	i.p. (6 mg/kg)
$t_{1/2}$ (h)	6.96 ± 0.97	5.84 ± 0.27
T_{max} (h)	−	0.83 ± 0.14
C_{max} (ng/mL)	−	178.4 ± 15.1
AUC_{0-24} (ng·h/mL)	333.5 ± 49.2	751.2 ± 54.8
$AUC_{0-\infty}$ (ng·h/mL)	347.2 ± 53.6	777.2 ± 59.7
AUC_{0-24}/D (ng·h/mL)	111.3 ± 16.0	125.2 ± 9.3
MRT $_{0-\infty}$ (h)	4.23 ± 0.43	5.30 ± 0.33
V_{ss} (mL/kg)	37.2 ± 7.4	−
CL (mL/min/kg)	147.4 ± 24.2	−
F (%)	−	112.2 ± 8.9

A mutant strain (KB002) of *S. flaveolus* was constructed by deleting the *mycB1-B4* genes using a CRISPR/Cas9 method (Supporting Information Fig. S4)[28]. The production of ansatrienins was completely abolished in strain KB002, which was successfully restored when fed with 3,5-AHBA (Fig. 8B). To screen for suitable mutasynthons for strain KB002, a series of 3,5-AHBA analogs aminobenzoates were supplemented into the *ΔmycB1-B4* mutant (Supporting Information Fig. S5). According to the HPLC analysis and the UV profile of ansatrienins, the four 3,5-AHBA analogs were successfully fed at relatively higher yields (Fig. 8B). Four analogs, including 3-amino-5-fluorobenzoic acid (3,5-AFBA), 3-amino-4-flurobenzonic acid (3,4-AFBA), 3-amino-5-methoxybenzonic acid (3,5-AMBA), and 3-amino-benzonic acid (3-ABA), were subsequently supplemented into KB002 in large-scale fermentation. Ultimately, 30 new derivatives, namely ansatrienins A1−A6, B1−B8, C1−C8, and D1−D8, were obtained by routine isolation and purification (Fig. 9A).

3.9. Structure characterization of new ansatrienin derivatives

Feeding with 3,5-AFBA resulted in the production of ansatrienins A1−A6 (Supporting Information Tables S4−S6 and Figs. S6−S11). The six new analogs were found to share a 22-fluorobenzene moiety, which was characterized by the ^{13}C NMR data (δ_C 164.2−164.4, d, C-22, $^1J_{C,F}$ = 242.2 Hz). The difference between ansatrienins A1−A6 lies in the substitution pattern of the C-30 side chain. In contrast to the common CHC unit, ansatrienins A1−A6 carry isobutyl (A1, A2), isopropyl (A3), 1-methylpropyl (A4), and isopentyl (A5, A6) groups at C-30. Ansatrienins A2 and A5 contain a C-25 hydroxymethyl group, which represents the first example in the ansatrienin family[41]. The formation of the C-25 hydroxymethyl group may be attributed to endogenous biotransformation in KB002, as no additional oxidoreductase genes are present within the *myc* BGC[16].

Supplementation of 3,4-AFBA into strain KB002 led to the isolation of ansatrienins B1−B8 (Supporting Information Tables S7−S11 and Figs. S12−S19). The eight ansatrienin derivatives possess a 21-fluorobenzene nucleus, which was established by the ^{13}C NMR data (δ_C 125.0−126.0, d, C-21, $^1J_{C,F}$ = 242.5 Hz). Like the ansatrienin A group (As), ansatrienins B1−B8 displayed different substitutions on the C-30 side chain, including isobutyl (B1, B2, B3), isopropyl (B4), 1-methylpropyl (B5), (*E*)-1-methylpropenyl (B6), isobutenyl (B7), and isopentyl (B8) groups, respectively. Ansatrienins B1 and B2 shared the same planar structure but differed in the geometry of the triene moiety. As the principal constituent of ansatrienin Bs, ansatrienin B1 exhibits a (4*E*, 6*E*, 8*E*)-geometry, which is a common feature of the majority of known ansatrienins. On the contrary, ansatrienin B2 had a (4*E*, 6*E*, 8*Z*)-geometry as indicated by a small coupling constant of $^3J_{8,9}$ (10.4 Hz) and an apparent shielded ^{13}C resonances of C-7 (δ_C 129.0 in B2; 133.7 in B1) and C-10 (δ_C 30.1 in B2; 33.9 in B1)[42]. Ansatrienin B3 had the same macrolactam structure as that of B1, but with the isobutanecarboxylalanine side chain attached at C-13 instead of C-11. The assignment was evidenced by the shielded ^{13}C

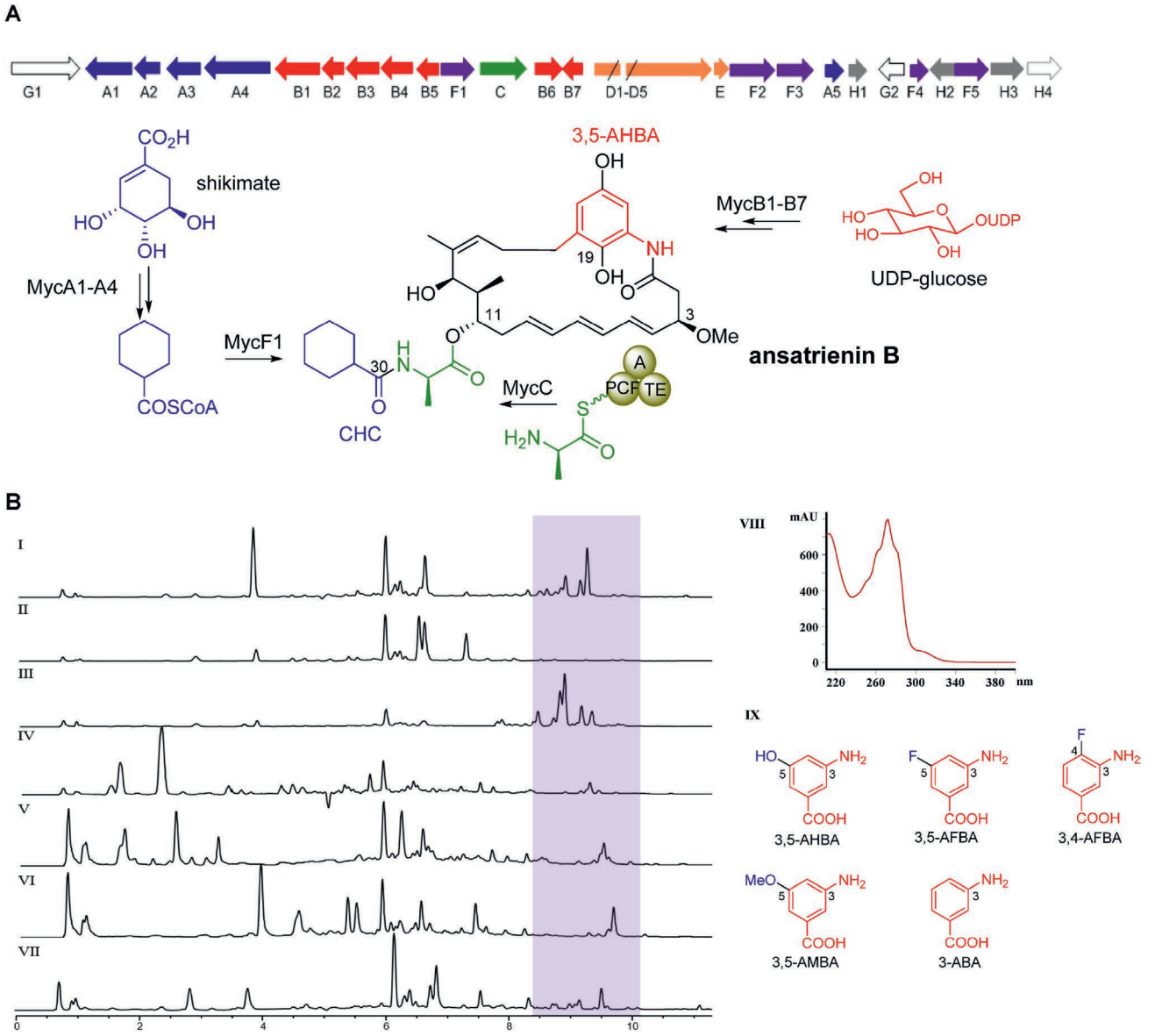

Figure 8 The proposed biosynthetic pathway of ansatrienin B and HPLC analyses of feeding experiments. (A) Proposed biosynthetic pathway of ansatrienins and the key precursors. (B) HPLC profile of ansatrienins production. I, *S. flaveolus* wide type; II, KB002; III, KB002 supplemented with 3,5-AHBA; IV, KB002 supplemented with 3,5-AFBA; VI, KB002 supplemented with 3,4-AFBA; V, KB002 supplemented with 3,5-AMBA; VII, KB002 supplemented with 3-ABA; VII, characterized UV profile of ansatrienins; IX, structures of feeding mutasynthons.

resonance for C-11 (δ_C 71.0 in B3 and δ_C 75.4 in B1) and the deshielded ^{13}C resonance for C-13 (δ_C 74.4 in B3 and δ_C 68.6 in B1). The shift of the side chain from C-11 to C-13 has been observed in trienomycin G and ansafurantrienin H[15,41].

Upon supplementation with 3,5-AMBA, the strain KB002 yielded eight ansatrienin derivatives, ansatrienins C1−C8 (Supporting Information Tables S12−S16 and Figs. S20−S27). Ansatrienins C1−C8 had an additional methoxy group (22-OMe), the presence of which is suggested by the ^1H and ^{13}C NMR resonances (δ_H 3.74−3.80 and δ_C 55.5−56.0). Ansatrienins C1, C2, and C7 contained a 22-methoxybenzene core, whereas ansatrienins C3, C4, C5, C6, and C8 contained a 19-hydroxyl-22-methoxybenzene moiety. Given that the 19-OH containing derivatives were only observed in ansatrienin Cs, it is proposed that 3,5-AMBA may be further recognized and oxidized by MycF2, resulting in the decoration of a 19-OH group[43]. The C-30 substituents in ansatrienins C1-C8 also exhibit a high structural diversity with isobutyl (C1, C3, C7, C8), isopropyl (C5), 1-methylpropyl (C2, C4), and isopentyl (C6) groups, respectively. Similar to ansatrienin B3, ansatrienins C7 and C8 had an isobutanecarboxylalanine chain attached to C-13 instead of to C-11.

When strain KB002 was fed with 3-ABA, eight ansatrienin derivatives, *i.e.*, ansatrienins D1−D8, were produced (Supporting Information Table S17−S21 and Figs. S28−S35). Ansatrienins D1−D8 did not have any substitutions on the benzene moiety, as confirmed by proton NMR resonances. The substituents at C-30 of ansatrienins D1−D8 included isobutyl (D1, D2, D8), isopropyl (D3), 1-methylpropyl (D4), (*E*)-1-methylpropenyl (D5), and isopentyl (D6, D7) groups. Ansatrienins D2 and D7 contained

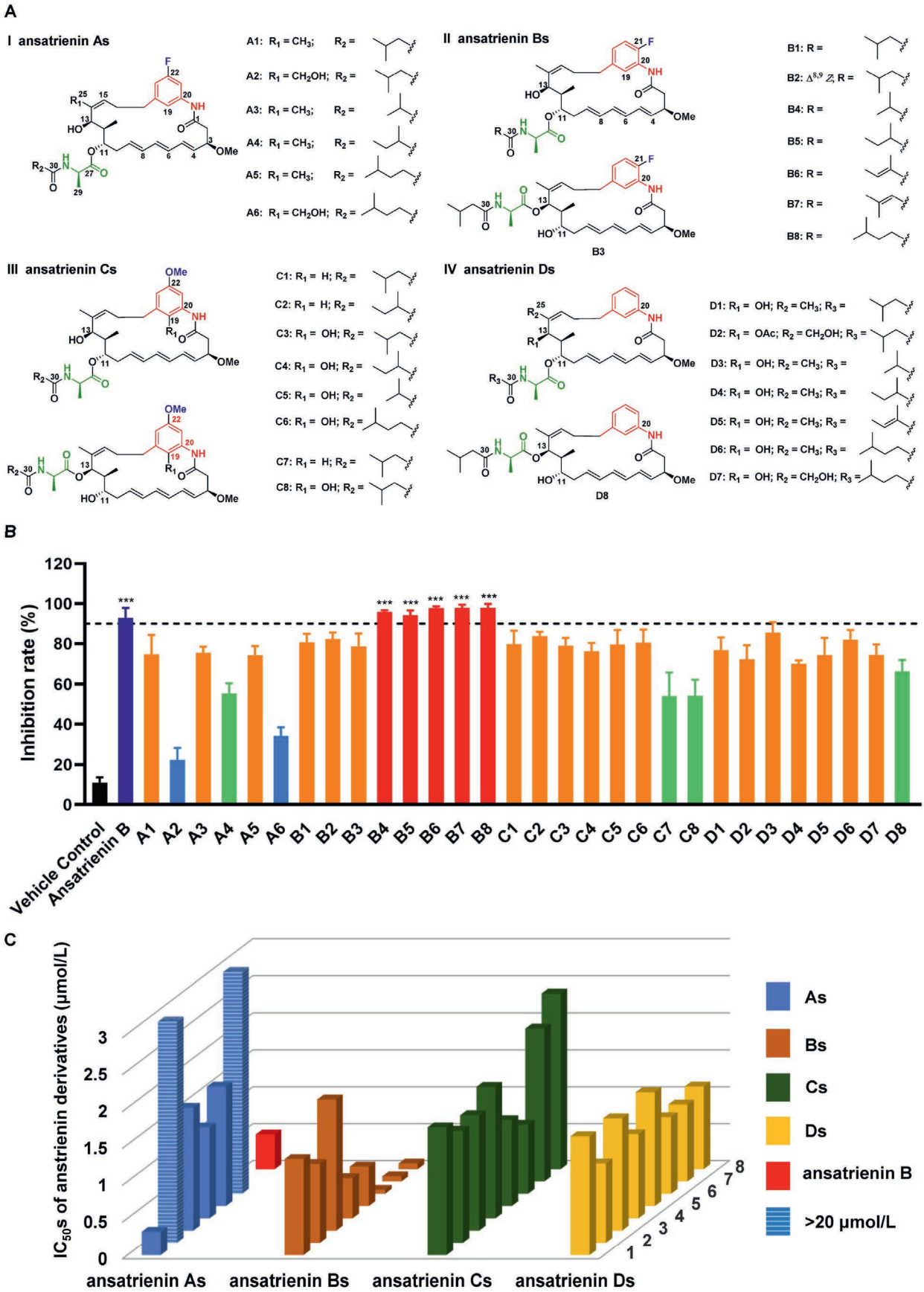
A
I ansatrienin As
A1: R1 = CH3; R2 =
A2: R1 = CH2OH; R2 =
A3: R1 = CH3; R2 =
A4: R1 = CH3; R2 =
A5: R1 = CH3; R2 =
A6: R1 = CH2OH; R2 =
II ansatrienin Bs
B1: R =
B2: Δ8,9 Z, R =
B4: R =
B5: R =
B6: R =
B7: R =
B8: R =
B3
III ansatrienin Cs
C1: R1 = H; R2 =
C2: R1 = H; R2 =
C3: R1 = OH; R2 =
C4: R1 = OH; R2 =
C5: R1 = OH; R2 =
C6: R1 = OH; R2 =
C7: R1 = H; R2 =
C8: R1 = OH; R2 =
IV ansatrienin Ds
D1: R1 = OH; R2 = CH3; R3 =
D2: R1 = OAc; R2 = CH2OH; R3 =
D3: R1 = OH; R2 = CH3; R3 =
D4: R1 = OH; R2 = CH3; R3 =
D5: R1 = OH; R2 = CH3; R3 =
D6: R1 = OH; R2 = CH3; R3 =
D7: R1 = OH; R2 = CH2OH; R3 =
D8
B
Inhibition rate (%)
120
100
80
60
40
20
0
***
Vehicle Control
Ansatrienin B
A1 A2 A3 A4 A5 A6 B1 B2 B3 B4 B5 B6 B7 B8 C1 C2 C3 C4 C5 C6 C7 C8 D1 D2 D3 D4 D5 D6 D7 D8
C
IC50s of anstrienin derivatives (μmol/L)
3
2.5
2
1.5
1
0.5
0
ansatrienin As
ansatrienin Bs
ansatrienin Cs
ansatrienin Ds
1 2 3 4 5 6 7 8
As
Bs
Cs
Ds
ansatrienin B
>20 μmol/L

a C-25 hydroxymethyl group, similar to ansatrienins A2 and A5. In addition, ansatrienin D2 had a C-13 acetyloxy group, which is rarely found in ansatrienins[41]. Ansatrienin D8 has a C-13 isobutanecarboxylalanine chain, which is similar to ansatrienins B3, C7, and C8.

3.10. Anti-SARS-CoV-2 activity of ansatrienin derivatives and SAR

Ansatrienin As−Ds were subjected to further testing for anti-SARS-CoV-2 activity on Vero E6 cells at 2.5 μmol/L. As shown in Fig. 9B, 24 derivatives showed potent activity, with an inhibition rate of more than 80%. Compared with ansatrienin B, most of ansatrienin As exhibited weaker antiviral activity (Fig. 9C and Supporting Information Fig. S36). Ansatrienin A2 and A6, which both possess a C-25 hydroxymethyl group, exhibited markedly diminished activities ($IC_{50} > 20$ μmol/L). Nevertheless, ansatrienins B1−B8 showed comparable or even superior antiviral activity relative to ansatrienin B. In particular, the IC_{50}s of ansatrienins B4−B8 were 0.5449, 0.5353, 0.05339, 0.07148, and 0.0775 μmol/L, respectively. The activities of ansatrienin B2 with (4*E*, 6*E*, 8*Z*) geometry and ansatrienin B3 with a C-13 acyl chain were weaker than those of the other ansatrienin Bs. The antiviral activities of ansatrienin Cs and Ds were found to be comparable with IC_{50}s ranging from 0.9372 to 2.378 μmol/L, but less than that of ansatrienin B. Of these, ansatrienin C7 and C8 were identified as the two least active derivatives. In summary, of the 30 new derivatives, ansatrienins B6−B8 exhibited the most potent anti-SARS-CoV-2 activities *in vitro*.

In the present study, a specific ansatrienin library was constructed, comprising 17 naturally occurring ansatrienins and 30 non-natural analogs generated *via* mutasynthesis. A preliminary SAR was delineated based on anti-SARS-CoV-2 activity (Fig. 1A and 9). First, it was established that the "molecular basket"-like skeleton of a 21-membered macrolactam was a crucial determinant of the anti-SARS-CoV-2 activity. Of the 17 natural ansatrienins, ansatrienins A, B, and 1c and trienomycins A and B exhibited sub-micromolar activity. In contrast, benzoxazomycin and ansafurantrienins, which lack the "molecular basket"-like skeleton, exhibited the lowest level of activity. Ansatrienin As−Ds contained a complete 21-membered macrolactam, and most of these compounds retained their anti-SARS-CoV-2 activity. Second, the types of benzenoid moieties (hydroquinone/quinone/phenol) in ansatrienins have been observed to exert minimal effects on activity, as exemplified by ansatrienins A and B and trienomycin A. The results of the mutasynthesis study facilitated the investigation of the impact of benzenoid substitution on antiviral activity. The 22-fluoro substitution has been observed to result in a reduction in antiviral activity (ansatrienin As), whereas the 21-fluoro substitution has been found to elicit an increase in activity (ansatrienin Bs). The 22-OMe group exerted a negligible influence on activity, as evidenced by the equipotent activities observed between ansatrienin Cs and ansatrienin B. Notably, the absence of substitution in the benzenoid also had a slight impact on activity. Ansatrienin Ds retained most of their activity, albeit with a slight reduction. Third, the acyl side chains of ansatrienins significantly influenced their activity. Ansatrienins with CHC-containing chains exhibited greater potency than those with small-molecule organic acid chains. Relocation of the acyl chain from C-11 to C-13 resulted in a notable reduction in the activity, as evidenced by ansatrienins B3, C7, C8, and D8. Furthermore, the C-25 hydroxymethyl group has been demonstrated to exert a detrimental impact on the activity, as seen in ansatrienins A2, A6, D2, and D7. To explain the different activities of the ansatrienin derivatives, docking studies were performed on ansatrienins A2, B1, and D1 (Supporting Information Fig. S37). A similar binding conformation to ansatrienin B was observed in the docking models of ansatrienins A2, B1, and D1. Notably, the 25-OH on ansatrienin A2 was mismatched in the hydrophobic pocket, showing incompatibility with the isopropyl group of the protein and the hydrophobic side chains of Leu576, Ala685, and Arg569. This may partially explain the weak activity of ansatrienin A2. Additionally, the docking scores predicted by AutoDock Vina were −0.854, −6.445, −7.653, and −7.450 kcal/mol for ansatrienins B, A2, B1, and D1, respectively, which is consistent with the weakest activity of ansatrienin A2.

4. Discussion

NPs have made significant contributions to new drug development owing to their unique structures and diverse bioactivities[44,45]. Ansatrienins, a group of 21-membered macrolactams, exhibit anticancer, antimicrobial, and anti-inflammatory activities *via* interactions with cellular targets such as epidermal growth factor receptor, signal transducer and activator of transcription-3, and eukaryotic elongation factor-1A (eEF1A)[41,46-48]. Here, we discovered for the first time that ansatrienin B has broad-spectrum activity at micromolar concentrations against SARS-CoV-2, Omicron variants, flaviviruses, and alphaviruses. Mechanistic studies demonstrated that ansatrienin B potentially affects both viral binding to the cell surface and viral replication. SPR affinity studies, molecular docking, RNA pull-down assays, and RdRp enzymatic activity assays (in gel, solution, and cellular forms) collectively confirmed that ansatrienin B directly interacts with RdRps of SARS-CoV-2 and WNV, disrupting both the binding of RdRp to viral RNA and its enzymatic activity. Furthermore, the antiviral activities of ansatrienin B were validated in animal models, where it efficiently inhibited SARS-CoV-2 and WNV infections. Ansatrienin B can significantly reduce the tissue viral load and alleviate pathological damage in mice, thereby mitigating weight loss or improving survival rate. Thirty new ansatrienin analogs were successively prepared by supplementation of 3,5-AHBA mutasynthons into the *S. flaveolus* mutant. Examination of anti-SARS-CoV-2 activity revealed four new candidates with enhanced anti-SARS-CoV-2 efficacy. Consequently, a preliminary SAR was established.

RdRp is functionally and structurally conserved across a wide range of RNA viruses and lacks a homologous counterpart in humans, making it an optimal target for the development of broad-spectrum inhibitors[49]. Inhibitors of SARS-CoV-2 RdRp are represented by nucleoside analog antivirals, such as remdesivir, molnupiravir, and favipiravir, which have the capacity to

Figure 9 Structures and of anti-SARS-CoV-2 efficacy of new ansatrienin derivatives. (A) Structures of ansatrienin derivatives As−Ds. (B) Anti-SARS-CoV-2 efficacy of ansatrienin derivatives As−Ds at 2.5 μmol/L in Vero E6 cells. (C) IC_{50}s of ansatrienin derivatives As−Ds against SARS-CoV-2 in Vero E6 cells. Data are represented as mean ± SD for three independent experiments. ***$P < 0.001$ compared to vehicle control.

terminate chain elongation and mutation of viral progeny[50]. A number of non-nucleoside inhibitors (NNIs) of RdRp have also been identified, including suramin, corilagin, and lycorine[51]. Ansatrienin B was identified in this study as a novel NNI of RdRp, which exhibited broad-spectrum antiviral activity against multiple viruses. Given that NPs typically exert their inhibitory effects on SARS-CoV-2 through multi-target or multi-pathway effects, it is plausible that the antiviral activity of ansatrienin B may be attributed to its potential effects on both the virus and the host[11]. Slight inhibition was observed when ansatrienin B was used during pretreatment (Fig. 3A), indicating a possible effect of ansatrienin B on host cells. Indeed, ansatrienin B has been demonstrated to exert inhibitory effects on eEF1A, which can interact with multiple viral proteins[47,52]. Plitidepsin, an eEF1A inhibitor, is currently examined in clinical trials for the treatment of COVID-19[53]. Moreover, ansatrienin B could inhibit SARS-CoV-2 binding without affecting the virions themselves or host factors during the entry stage (Fig. 3B, C, and Fig. S3), suggesting that the inhibitory effect may occur during the virus-host interaction, the specific mechanism, however, warrants further exploration.

The ansamycin biosynthetic assembly utilizes 3,5-AHBA as the starter unit, which can be replaced by various 3,5-AHBA-like mutasynthons[54]. A series of mutasynthetic studies have been carried out on ansamycins such as ansamitocin[38,39,55-58], geldanamcin[40,56,59], reblastatin[60], and rifamycin[61], yielding a number of unusual derivatives, encompassing atypical scaffolds with alicyclic (*e.g.,* halo-, azido-substitution) or heterocyclic (*e.g.*, thiazole, thiazine, benzotriazole, heterocyclic) aromatic cores. The current results demonstrate that artificial benzoates can also be incorporated into ansatrienin biosynthesis, with the successful generation of 30 new derivatives. A total of 80 ansatrienins have been documented before the present investigation[41]. Our study thus makes a substantial contribution to the expansion of the ansatrienin family.

The structural diversity of ansatrienins is mainly attributed to the diverse moieties of the aromatic core and side chains. The C-30 side chains of ansatrienin As−Ds displayed a remarkable degree of diversity, indicating the presence of multiple short-chain acyl groups. Unloading of the C-30 acyl groups of ansatrienins is catalyzed by MycF1, an *N*-acyltransferase. The diverse C-30 acyl substituents in ansatrienin As - Ds are related to the remarkable substrate tolerance of MycF1, which can accept CHC acid, as well as a range of small-molecule organic acids[62,63]. During feeding experiments, small-molecule organic acids, which typically originate from primary metabolism, are incorporated into ansatrienin biosynthesis. Notably, none of the ansatrienin As−Ds contained a CHC moiety. The genes responsible for the biosynthesis of 3,5-AHBA and CHC are mutually independent in *myc* BGC[16,17]. It is hypothesized that the CHC moiety is derived from a shikimic acid (SA). The conversion of SA into CHC-CoA involves a series of reduction and dehydration steps. The biosynthesis of SA has been well documented in bacteria[64]. The three enzymatic steps that originate from D-erythrose-4-phosphate (E4P) to 3-dehydroshikimate (DHS) are highly similar to those observed in the 3,5-AHBA biosynthetic pathway, which yields aminoDHS (Supporting Information Fig. S38). These enzymes, namely 3-deoxy-D-arabino-heptulosonate-7-phosphate (DAHP) synthase, 3-dehydroquinate (DHQ) synthase, and DHQ dehydratase, exhibit homology to MycB1, MycB7, and MycB5, respectively. The reason for the disruption of the production of the CHC moiety is unclear. It seems reasonable to posit that the deletion of mycB1-B4 has the unintended consequence of disrupting the biosynthesis of both 3,5-AHBA and CHC. In short, the supplementation of 3,5-AHBA-derived mutasynthons into the *ΔmycB1-B4* mutant resulted in the generation of diversified ansatrienin derivatives with both non-natural aromatic cores and modifiable C-11 dipeptidyl motifs.

5. Conclusions

The present study identified ansatrienin B as a promising broad-spectrum antiviral agent with *in vitro* activity against multiple RNA viruses, including SARS-CoV-2, Omicron variants, flaviviruses, and alphaviruses, and *in vivo* efficacy against SARS-CoV-2 and WNV. The antiviral activity of ansatrienin B is attributed to its ability to interact with RdRps and suppress its enzymatic activity, thereby inhibiting viral replication. Mutasynthesis has been demonstrated to be an efficacious approach for the generation of a specific ansatrienin library and the facilitation of SAR analysis. These findings present a prospective candidate for further development as an antiviral agent.

Acknowledgments

We thank professor Zhigang Yi of Fudan University for helping with SARS-CoV-2 replicon. This work was financially supported by the National Key Research and Development Program of China (2022YFC2804105 and 2019YFC0312502), and the National Natural Science Foundation of China (82273849, 81622044, 32171189, 32000223, and 32300138), and the Strategic Priority Research Program of the Chinese Academy of Sciences Grant (XDA0530000).

Author contributions

Peng Sun, Yangang Liu, and Ping Zhao conceptualized the study; Xu Zheng, Hongji Li, Mengxue Zhang, Zhiyue Qiu, Xingchi Yang, Ziwei Zhou, Wei Wu, Dunning Yu, Xiaofan, Zhu, Haoran Peng, and Cuiling Ding performed the experiments; Xu Zheng, Hongji Li, and Zhiyue Qiu analyzed the data; Xu Zheng, Hongji Li, and Peng Sun wrote the original draft; Zhiyong Chu, Wen Liu, Wanchao Yin, Peng Sun, and Yangang Liu provided resources and revised the final draft; All authors have read and approved the final manuscript.

Conflicts of interest

The authors declare no competing interest.

Appendix A. Supporting information

Supporting information to this article can be found online at https://doi.org/10.1016/j.apsb.2026.02.021.

References

1. Nandu TG, Jithesh K. Natural product-based anti-viral agents against RNA viruses: an important strategy for pandemic preparedness. In: *Drugs from nature: targets, assay systems and leads*. Springer; 2024. p. 411−40.
2. Phillips N. The coronavirus is here to stay−here's what that means. *Nature* 2021;**590**:382−4.

3. Habarugira G, Suen WW, Hobson-Peters J, Hall RA, Bielefeldt-Ohmann H. West Nile virus: an update on pathobiology, epidemiology, diagnostics, control and "One Health" implications. *Pathogens* 2020; **9**:589.
4. Pierson TC, Diamond MS. The continued threat of emerging flaviviruses. *Nat Microbiol* 2020;**5**:796−812.
5. Zaid A, Burt FJ, Liu X, Poo YS, Zandi K, Suhrbier A, et al. Arthritogenic alphaviruses: epidemiological and clinical perspective on emerging arboviruses. *Lancet Infect Dis* 2021;**21**:e123−33.
6. Li G, Hilgenfeld R, Whitley R, De Clercq E. Therapeutic strategies for COVID-19: progress and lessons learned. *Nat Rev Drug Discov* 2023; **22**:449−75.
7. Chan CC-Y, Guo Q, Chan JF-W, Tang K, Cai J-P, Chik KK-H, et al. Identification of novel small-molecule inhibitors of SARS-CoV-2 by chemical genetics. *Acta Pharm Sin B* 2024;**14**:4028−44.
8. Xie Y, Yin W, Zhang Y, Shang W, Wang Z, Luan X, et al. Design and development of an oral remdesivir derivative VV116 against SARS-CoV-2. *Cell Res* 2021;**31**:1212−4.
9. Christy MP, Uekusa Y, Gerwick L, Gerwick WH. Natural products with potential to treat RNA virus pathogens including SARS-CoV-2. *J Nat Prod* 2021;**84**:161−82.
10. Szabó D, Crowe A, Mamotte C, Strappe P. Natural products as a source of coronavirus entry inhibitors. *Front Cell Infect Microbiol* 2024;**14**:1353971.
11. Zhao Y, Deng S, Bai Y, Guo J, Kai G, Huang X, et al. Promising natural products against SARS-CoV-2: structure, function, and clinical trials. *Phytother Res* 2022;**36**:3833−58.
12. Thomas E, Stewart LE, Darley BA, Pham AM, Esteban I, Panda SS. Plant-based natural products and extracts: potential source to develop new antiviral drug candidates. *Molecules* 2021;**26**: 6197.
13. Skrzypczak N, Przybylski P. Structural diversity and biological relevance of benzenoid and atypical ansamycins and their congeners. *Nat Prod Rep* 2022;**39**:1678−704.
14. Skrzypczak N, Przybylski P. Modifications, biological origin and antibacterial activity of naphthalenoid ansamycins. *Nat Prod Rep* 2022;**39**:1653−77.
15. Li H, Chen S, Wang J, Zhang M, Wu W, Liu W, et al. Ansafurantrienins, unprecedented ansatrienin derivatives formed *via* photocatalytic intramolecular [3 + 2] oxidative cycloaddition. *Org Lett* 2022;**24**:592−6.
16. Qu X, Lei C, Liu W. Transcriptome mining of active biosynthetic pathways and their associated products in *Streptomyces flaveolus*. *Angew Chem Int Ed Engl* 2011;**50**:9651−4.
17. Kang Q, Shen Y, Bai L. Biosynthesis of 3,5-AHBA-derived natural products. *Nat Prod Rep* 2012;**29**:243−63.
18. Ren Y, Min YQ, Liu M, Chi L, Zhao P, Zhang XL. *N*-Glycosylation-mutated HCV envelope glycoprotein complex enhances antigen-presenting activity and cellular and neutralizing antibody responses. *Biochim Biophys Acta* 2016;**1860**:1764−75.
19. Liu SH, Wei YY, Xing YN, Chen Y, Wang W, Wang KB, et al. A BBE-like oxidase, AsmF, dictates the formation of naphthalenic hydroxyl groups in ansaseomycin biosynthesis. *Org Lett* 2021;**23**: 3724−8.
20. Yin W, Mao C, Luan X, Shen DD, Shen Q, Su H, et al. Structural basis for inhibition of the RNA-dependent RNA polymerase from SARS-CoV-2 by remdesivir. *Science* 2020;**368**:1499−504.
21. Yin W, Luan X, Li Z, Zhou Z, Wang Q, Gao M, et al. Structural basis for inhibition of the SARS-CoV-2 RNA polymerase by suramin. *Nat Struct Mol Biol* 2021;**28**:319−25.
22. Zhao J, Guo S, Yi D, Li Q, Ma L, Zhang Y, et al. A cell-based assay to discover inhibitors of SARS-CoV-2 RNA dependent RNA polymerase. *Antivir Res* 2021;**190**:105078.
23. Qian X, Wu B, Tang H, Luo Z, Xu Z, Ouyang S, et al. Rifapentine is an entry and replication inhibitor against yellow fever virus both *in vitro* and *in vivo*. *Emerg Microb Infect* 2022;**11**:873−84.
24. Trott O, Olson AJ. AutoDock Vina: improving the speed and accuracy of docking with a new scoring function, efficient optimization, and multithreading. *J Comput Chem* 2010;**31**:455−61.
25. Delano WL. PyMOL: an open-source molecular graphics tool. *CCP4 Newslett Prot Crystallogr* 2002;**40**:82−92.
26. Ravindranath PA, Forli S, Goodsell DS, Olson AJ, Sanner MF. AutoDockFR: advances in protein−ligand docking with explicitly specified binding site flexibility. *PLoS Comput Biol* 2015;**11**:e1004586.
27. Francis ME, Goncin U, Kroeker A, Swan C, Ralph R, Lu Y, et al. SARS-CoV-2 infection in the Syrian hamster model causes inflammation as well as type I interferon dysregulation in both respiratory and non-respiratory tissues including the heart and kidney. *PLoS Pathog* 2021;**17**:e1009705.
28. Mo J, Wang S, Zhang W, Li C, Deng Z, Zhang L, et al. Efficient editing DNA regions with high sequence identity in actinomycetal genomes by a CRISPR-Cas9 system. *Syn Syst Biotechno* 2019;**4**:86−91.
29. Wang Y, Wang Y, Chu J, Zhuang Y, Zhang L, Zhang S. Improved production of erythromycin A by expression of a heterologous gene encoding *S*-adenosylmethionine synthetase. *Appl Microbiol Biotechnol* 2007;**75**:837−42.
30. Miao G, Peng H, Tang H, Liu Y, Zheng X, Liu B, et al. Antiviral efficacy of selective estrogen receptor modulators against SARS-CoV-2 infection *in vitro* and *in vivo* reveals bazedoxifene acetate as an entry inhibitor. *J Med Virol* 2022;**94**:4809−19.
31. Peng H, Ding C, Jiang L, Tang W, Liu Y, Zhao L, et al. Discovery of potential anti-SARS-CoV-2 drugs based on large-scale screening *in vitro* and effect evaluation *in vivo*. *Sci China Life Sci* 2022;**65**: 1181−97.
32. Goc A, Sumera W, Rath M, Niedzwiecki A. Linoleic acid binds to SARS-CoV-2 RdRp and represses replication of seasonal human coronavirus OC43. *Sci Rep* 2022;**12**:19114.
33. Vial T, Oade MS, Russell CA, Eggink D, te Velthuis AJW. A SARS-CoV-2 mini-genome assay based on negative-sense RNA to study replication inhibitors and emerging mutations. *bioRxiv* 2021. 2021.06.28.450211.
34. Chen X, Ding L, Tao Y, Pannecouque C, De Clercq E, Zhuang C, et al. Bioisosterism-based design and enantiomeric profiling of chiral hydroxyl-substituted biphenyl-diarylpyrimidine nonnucleoside HIV-1 reverse transcriptase inhibitors. *Eur J Med Chem* 2020;**202**:112549.
35. Imai H, Uchiumi T, Kodera N. Direct visualization of translational GTPase factor pool formed around the archaeal ribosomal P-stalk by high-speed AFM. *Proc Natl Acad Sci U S A* 2020;**117**:32386−94.
36. Sia SF, Yan LM, Chin AWH, Fung K, Choy KT, Wong AYL, et al. Pathogenesis and transmission of SARS-CoV-2 in golden hamsters. *Nature* 2020;**583**:834−8.
37. Nair AB, Jacob S. A simple practice guide for dose conversion between animals and human. *J Basic Clin Pharm* 2016;**7**:27−31.
38. Taft F, Brunjes M, Floss HG, Czempinski N, Grond S, Sasse F, et al. Highly active ansamitocin derivatives: mutasynthesis using an AHBA-blocked mutant. *Chembiochem* 2008;**9**:1057−60.
39. Knobloch T, Harmrolfs K, Taft F, Thomaszewski B, Sasse F, Kirschning A. Mutational biosynthesis of ansamitocin antibiotics: a diversity-oriented approach to exploit biosynthetic flexibility. *Chembiochem* 2011;**12**:540−7.
40. Hermane J, Eichner S, Mancuso L, Schroder B, Sasse F, Zeilinger C, et al. New geldanamycin derivatives with anti Hsp properties by mutasynthesis. *Org Biomol Chem* 2019;**17**:5269−78.
41. Yang X, Wu W, Li H, Zhang M, Chu Z, Wang X, et al. Natural occurrence, bioactivity, and biosynthesis of triene-ansamycins. *Eur J Med Chem* 2022;**244**:114815.
42. Seidman K, Maciel GE. Proximity and conformational effects on ^{13}C chemical shifts at the γ position in hydrocarbons. *J Am Chem Soc* 1977;**99**:659−71.
43. Ye F, Zhao X, Shi Y, Hu Y, Ding Y, Lu C, et al. Deciphering the timing of naphthalenic ring formation in the biosynthesis of 8-deoxyrifamycins. *Org Lett* 2023;**25**:6474−8.

44. Tian WJ, Wang XJ. Broad-spectrum antivirals derived from natural products. *Viruses* 2023;**15**:1100.
45. Martinez JP, Sasse F, Brönstrup M, Diez J, Meyerhans A. Antiviral drug discovery: broad-spectrum drugs from nature. *Nat Prod Rep* 2015; **32**:29−48.
46. Carelli JD, Sethofer SG, Smith GA, Miller HR, Simard JL, Merrick WC, et al. Ternatin and improved synthetic variants kill cancer cells by targeting the elongation factor-1A ternary complex. *eLife* 2015;**4**:e10222.
47. Sánchez-Murcia PA, Cortés-Cabrera Á, Gago F. Structural rationale for the cross-resistance of tumor cells bearing the A399V variant of elongation factor eEF1A1 to the structurally unrelated didemnin B, ternatin, nannocystin A and ansatrienin B. *J Comput Aided Mol Des* 2017;**31**:915−28.
48. Brönstrup M, Sasse F. Natural products targeting the elongation phase of eukaryotic protein biosynthesis. *Nat Prod Rep* 2020;**37**:752−62.
49. Cannalire R, Cerchia C, Beccari AR, Di Leva FS, Summa V. Targeting SARS-CoV-2 proteases and polymerase for COVID-19 treatment: state of the art and future opportunities. *J Med Chem* 2022;**65**:2716−46.
50. Jin YH, Min JS, Jeon S, Lee J, Kim S, Park T, et al. Lycorine, a non-nucleoside RNA dependent RNA polymerase inhibitor, as potential treatment for emerging coronavirus infections. *Phytomedicine* 2021; **86**:153440.
51. Dejmek M, Konkoľová E, Eyer L, Straková P, Svoboda P, Šála M, et al. Non-nucleotide RNA-dependent RNA polymerase inhibitor that blocks SARS-CoV-2 replication. *Viruses* 2021;**13**:1585.
52. Snape N, Li D, Wei T, Jin H, Lor M, Rawle DJ, et al. The eukaryotic translation elongation factor 1A regulation of actin stress fibers is important for infectious RSV production. *Virol J* 2018;**15**:182.
53. White KM, Rosales R, Yildiz S, Kehrer T, Miorin L, Moreno E, et al. Plitidepsin has potent preclinical efficacy against SARS-CoV-2 by targeting the host protein eEF1A. *Science* 2021;**371**: 926−31.
54. Admiraal SJ, Walsh CT, Khosla C. The loading module of rifamycin synthetase is an adenylation-thiolation didomain with substrate tolerance for substituted benzoates. *Biochemistry* 2001;**40**: 6116−23.
55. Eichner S, Knobloch T, Floss HG, Fohrer J, Harmrolfs K, Hermane J, et al. The interplay between mutasynthesis and semisynthesis: generation and evaluation of an ansamitocin library. *Angew Chem Int Ed Engl* 2012;**51**:752−7.
56. Mancuso L, Jurjens G, Hermane J, Harmrolfs K, Eichner S, Fohrer J, et al. Bioreduction of aryl azides during mutasynthesis of new ansamitocins. *Org Lett* 2013;**15**:4442−5.
57. Wang LL, Balakrishnan A, Bigall NC, Candito D, Miethe JF, Seidel K, et al. A bio-chemosynthetic approach to superparamagnetic iron oxide-ansamitocin conjugates for use in magnetic drug targeting. *Chem Eur J* 2017;**23**:2265−70.
58. Wesemann F, Heutling A, Wienecke P, Kirschning A. First ring-expanded maytansin lactone accessed by a new mutasynthetic variant. *Chembiochem* 2020;**21**:2927−30.
59. Hermane J, Bulyszko I, Eichner S, Sasse F, Collisi W, Poso A, et al. New, non-quinone fluorogeldanamycin derivatives strongly inhibit Hsp90. *Chembiochem* 2015;**16**:302−11.
60. Mohammadi-Ostad-Kalayeh S, Stahl F, Scheper T, Kock K, Herrmann C, Heleno Batista FA, et al. Heat shock proteins revisited: using a mutasynthetically generated reblastatin library to compare the inhibition of human and leishmania Hsp90s. *Chembiochem* 2018;**19**:562−74.
61. Bulyszko I, Drager G, Klenge A, Kirschning A. Evaluation of the synthetic potential of an AHBA knockout mutant of the rifamycin producer *Amycolatopsis mediterranei*. *Chem Eur J* 2015;**21**: 19231−42.
62. Shi G, Shi N, Li Y, Chen W, Deng J, Liu C, et al. D-Alanylation in the assembly of ansatrienin side shain is catalyzed by a modular NRPS. *ACS Chem Biol* 2016;**11**:876−81.
63. Song YN, Jiao RH, Zhang WJ, Zhao GY, Dou H, Jiang R, et al. New ansamycin derivatives generated by simultaneous mutasynthesis. *Org Lett* 2015;**17**:556−9.
64. Skyrud W, Flores ADR, Zhang W. Biosynthesis of cyclohexanecarboxyl-CoA highlights a promiscuous shikimoyl-CoA synthetase and a FAD-dependent dehydratase. *ACS Catal* 2020;**10**:3360−4.